1 **A human antibody that broadly neutralizes betacoronaviruses protects**
2 **against SARS-CoV-2 by blocking the fusion machinery**

3 Dora Pinto[1*], Maximilian M. Sauer[2*], Nadine Czudnochowski[3*], Jun Siong Low[4*], M. Alejandra Tortorici[2],
4 Michael P. Housley[3], Julia Noack[3], Alexandra C. Walls[2], John E. Bowen[2], Barbara Guarino[1], Laura E.
5 Rosen[3], Julia di Iulio[3], Josipa Jerak[4], Hannah Kaiser[3], Saiful Islam[3], Stefano Jaconi[1], Nicole Sprugasci[1],
6 Katja Culap[1], Rana Abdelnabi[5], Caroline Foo[5], Lotte Coelmont[5], Istvan Bartha[1], Siro Bianchi[1], Chiara
7 Silacci-Fregni[1], Jessica Bassi[1], Roberta Marzi[1], Eneida Vetti[1], Antonino Cassotta[4], Alessandro Ceschi [6,7,8,9],
8 Paolo Ferrari [9,10,11], Pietro E. Cippà [10,12], Olivier Giannini[9,10], Samuele Ceruti[13], Christian Garzoni[14], Agostino
9 Riva[15], Fabio Benigni[1], Elisabetta Cameroni[1], Luca Piccoli[1], Matteo S. Pizzuto[1], Megan Smithey[3], David
10 Hong[3], Amalio Telenti[3], Florian A. Lempp[3], Johan Neyts[5], Colin Havenar-Daughton[3], Antonio
11 Lanzavecchia[1], Federica Sallusto[4,16], Gyorgy Snell[3], Herbert W. Virgin[3,17,18], Martina Beltramello[1], Davide
12 Corti[1#] and David Veesler[2#]

13
14 [1]Humabs Biomed SA, a subsidiary of Vir Biotechnology, 6500 Bellinzona, Switzerland
15 [2]Department of Biochemistry, University of Washington, Seattle, Washington 98195, USA
16 [3]Vir Biotechnology, San Francisco, CA 94158, USA
17 [4]Institute for Research in Biomedicine, Università della Svizzera italiana, 6500 Bellinzona, Switzerland
18 [5]Rega Institute for Medical Research, Laboratory of Virology and Chemotherapy, KU Leuven, 3000 Leuven, Belgium
19 [6]Clinical Trial Unit, Ente Ospedaliero Cantonale, 6900 Lugano, Switzerland
20 [7]Division of Clinical Pharmacology and Toxicology, Institute of Pharmacological Sciences of Southern Switzerland,
21 Ente Ospedaliero Cantonale, 6900 Lugano, Switzerland
22 [8]Department of Clinical Pharmacology and Toxicology, University Hospital Zurich, 8091 Zurich, Switzerland
23 [9]Faculty of Biomedical Sciences, Università della Svizzera italiana, 6900 Lugano, Switzerland
24 [10]Department of Medicine, Ente Ospedaliero Cantonale, 6500 Bellinzona, Switzerland
25 [11]Clinical School, University of New South Wales, 2052 Sydney, Australia
26 [12]Faculty of Medicine, University of Zurich, 8057 Zurich, Switzerland
27 [13] Intensive Care Unit, Clinica Luganese Moncucco, 6900 Lugano, Switzerland
28 [14]Clinic of Internal Medicine and Infectious Diseases, Clinica Luganese Moncucco, 6900 Lugano, Switzerland
29 [15]III Division of Infectious Diseases, ASST Fatebenefratelli Sacco, Luigi Sacco Hospital, 20157 Milan, Italy
30 [16]Institute of Microbiology, ETH Zurich, 8093 Zurich, Switzerland
31 [17]UT Southwestern Medical Center, Dallas, TX, 75390 USA
32 [18]Washington University School of Medicine, St. Louis, MO, 63110 USA
33
34
35 [*]These authors contributed equally
36
37 [#]Correspondence: dveesler@uw.edu, dcorti@vir.bio
38

39 **The repeated spillovers of β-coronaviruses in humans along with the rapid emergence of**
40 **SARS-CoV-2 escape variants highlight the need to develop broad coronavirus therapeutics**
41 **and vaccines. Five monoclonal antibodies (mAbs) were isolated from COVID-19**
42 **convalescent individuals and found to cross-react with multiple β-coronavirus spike (S)**
43 **glycoproteins by targeting the stem helix. One of these mAbs, S2P6, cross-reacts with**
44 **more than twenty human and animal β-coronavirus S glycoproteins and broadly**
45 **neutralizes SARS-CoV-2 and pseudotyped viruses from the sarbecovirus, merbecovirus**
46 **and embecovirus subgenera. Structural and functional studies delineate the molecular**
47 **basis of S2P6 cross-reactivity and broad neutralization and indicate that this mAb blocks**
48 **viral entry by inhibiting membrane fusion. S2P6 protects hamsters challenged with SARS-**
49 **CoV-2 (including the B.1.351 variant of concern) through direct viral neutralization and Fc-**
50 **mediated effector functions. Serological and B cell repertoire analyses indicate that**
51 **antibodies targeting the stem helix are found in some convalescent donors and vaccinees**
52 **but are predominantly of narrow specificity. Germline reversion of the identified cross-**
53 **reactive mAbs revealed that their unmutated ancestors are specific for the endemic OC43**
54 **or HKU1 viruses and acquired enhanced affinity and breadth through somatic mutations.**
55 **These data demonstrate that conserved epitopes in the coronavirus fusion machinery can**
56 **be targeted by protective antibodies and provide a framework for structure-guided design**
57 **of pan-β-coronavirus vaccines eliciting broad protection.**

58
59

60 **Introduction**

61

62   Severe acute respiratory syndrome coronavirus 2 (SARS-CoV-2), which is the causative
63 agent of the coronavirus disease 2019 (COVID-19), emerged at the end of 2019 and seeded the
64 ongoing pandemic (*1*). Coronaviruses are zoonotic pathogens found in avian and mammalian
65 reservoirs, including bats, palm civets, racoon dogs, pangolins and pigs to cite a few. Repeated
66 spillovers to humans demonstrates that these viruses have broad capability to spread between
67 multiple phylogenetically distinct species. Over the past two decades, in addition to SARS-CoV-
68 2, severe acute respiratory syndrome coronavirus (SARS-CoV) and Middle-East respiratory
69 syndrome coronavirus (MERS-CoV) crossed the species barrier to humans leading to epidemics.
70 All three highly pathogenic coronaviruses belong to the β-coronavirus genus: SARS-CoV-2 and
71 SARS-CoV cluster within lineage B (*sarbecovirus* subgenus) and likely originated in bats whereas
72 MERS-CoV belongs to lineage C (*merbecovirus* subgenus) and is transmitted to humans via
73 contact with dromedary camels. Furthermore, four endemic coronaviruses cause common colds
74 in humans: the HCoV-HKU1 and HCoV-OC43 β-coronaviruses in lineage A (*embecovirus*
75 subgenus) and the more distantly related α-coronaviruses NL63 and 229E (*setracovirus* and
76 *duvinacovirus* subgenus).
77   The coronavirus spike (S) glycoprotein promotes viral entry into host cells through an S_1
78 subunit which engages host receptors and an S_2 subunit involved in membrane fusion (*2*). The
79 S_1 subunit mediates receptor attachment, is the major target of (neutralizing) antibodies (Abs),
80 and harbors the most sequence variability within the S glycoprotein (*3–6*). Accordingly, Abs
81 binding to the receptor-binding domain (RBD) and N-terminal domain (NTD within the S_1 subunit
82 exert a selective pressure resulting in the emergence of new variants (*6–10*). The S_2 subunit is

83   more conserved than the S_1 subunit among coronaviruses putatively due to the necessity to
84   maintain the functionality of the fusion machinery and due to low immune pressure. The extensive
85   glycan shield on the S_2 subunit is also conserved among coronaviruses while retaining
86   accessibility to functionally important regions, such as the fusion peptide (*11*). Abs binding to the
87   S_2 fusion machinery could potentially neutralize distantly related coronaviruses as reported for
88   human and mouse mAbs (*12–14*) and observed for other viruses, such as influenza and HIV-1
89   (*15, 16*).
90   The emergence and rapid spread of SARS-CoV-2 has unequivocally demonstrated the
91   need to develop interventions against coronaviruses, for this pandemic as well as for future
92   spillover events. In the long term, the most effective drugs will be those with efficacy against a
93   broad spectrum of coronaviruses, such as broadly neutralizing mAbs which target highly
94   conserved S epitopes that are less likely to mutate and develop resistance. Furthermore,
95   identifying conserved epitopes may guide the design of next generation pan β-coronavirus
96   vaccines that could protect against both current and future emerging SARS-CoV-2 variants and
97   other β-coronaviruses.
98   Here we describe the isolation of five mAbs that cross-react and broadly neutralize
99   multiple human and animal β-coronaviruses by targeting the S glycoprotein stem helix. Structural
100 and functional analyses of one of these mAbs (S2P6) indicate that inhibition of viral entry involves
101 blocking membrane fusion which is the basis for broad β-coronavirus neutralization. S2P6
102 activates immune cell-dependent effector functions in vitro and protects hamsters challenged with
103 SARS-CoV-2 Wuhan-1 and B.1.351 isolates leveraging both neutralization and effector functions.
104 These findings pave the way for the development of pan β-coronavirus vaccines and therapeutics.
105
106
107 **Results**
108
109 **Isolation of a broadly-neutralizing β-coronavirus mAb from a convalescent SARS-CoV-2**
110 **exposed individual**
111   To identify mAbs targeting highly conserved regions of the S glycoprotein, we interrogated
112 human IgG$^+$ memory B cells from three COVID-19 convalescent donors. Five mAbs bound to the
113 prefusion-stabilized S ectodomain trimers of viruses belonging to all three human-infecting β-
114 coronavirus subgenera, i.e., *sarbecovirus* (SARS-CoV and SARS-CoV-2), *merbecovirus* (MERS-
115 CoV) and *embecovirus* (OC43 and HKU1), but not to the human α-coronaviruses (229E and
116 NL63) (**Fig. 1A-C** and **fig. S1A-B**). S2P6 and S2S43 mAbs were derived from two donors and
117 use VH1-46*01 and D5-12*01 genes whereas the other 3 mAbs (P34D10, P34G12 and P34E3),
118 derived from a third donor, are clonally related and use the VH3-30 gene (**fig. S1A**). Overall, the
119 level of somatic mutations in these 5 mAbs in variable regions was moderate with nucleotide
120 sequence identities to germline genes ranging from 86 to 97% (**fig. S1A**). The mAbs bound to
121 both prefusion and post-fusion SARS-CoV-2 S with comparable apparent avidities, indicating that
122 their cognate epitope is (at least partially) accessible in both conformational states of the S
123 glycoprotein (**Fig. 1A** and **fig. S1B-C**).
124   S2P6 was selected for further in-depth characterization and shown to bind to all full-length
125 SARS-CoV-2 S variants tested and to 25 S glycoproteins (transiently expressed on the surface
126 of ExpiCHO cells) representative of all *sarbecovirus* clades (**Fig. 1D** and **fig. S1D-E**). Using

127 surface plasmon resonance (SPR), we found that S2P6 Fab fragment had the highest affinity for
128 SARS-CoV-2 S and SARS-CoV S followed by MERS-CoV S and OC43 S with equilibrium
129 dissociation constants (K_D) of 7, 7, 12 and 16 nM, respectively (**fig. S1F-G**). S2P6 also bound to
130 HKU1 S albeit with reduced affinity (K_D ~120 nM) (**fig. S1F**). The recognition of prefusion SARS-
131 CoV-2 S by this mAb is pH dependent with higher binding affinity at pH 7, relative to pH 5, in both
132 IgG and Fab formats (**fig. S1G**). Together, these data demonstrate the remarkable and efficient
133 cross-reactivity of S2P6 towards all human-infecting β-coronaviruses.
134   To evaluate the neutralization potency and breadth of S2P6, we investigated its ability to
135 inhibit entry of authentic SARS-CoV-2 into Vero-E6 cells in the presence or absence of the S-
136 activating protease TMPRSS2. S2P6 completely neutralized infection of TMPRSS2-positive
137 Vero-E6 cells but was less effective in neutralizing infection of Vero-E6 cells (**Fig. 1E**). Previous
138 studies established that the main route of SARS-CoV-2 entry into cultured lung cells occurs
139 through TMPRSS2-activated fusion with the cytoplasmic membrane (*17–19*). The more efficient
140 S2P6-mediated neutralization of SARS-CoV-2 entry into Vero-E6 cells expressing TMPRSS2,
141 relative to cells lacking this protease, would be consistent with reduced S2P6 binding at
142 endosomal pH (**fig. S1G)** and suggests that S2P6 is maximally efficient towards the viral entry
143 pathway associated with lung cell infection. We subsequently assessed S2P6-mediated
144 neutralization of vesicular stomatitis virus (VSV) (*20*) pseudotyped with SARS-CoV-2 S of several
145 variants of concern (VOC), including B.1.1.7, B.1.351 and P.1, and observed similar potency to
146 that found against the parental SARS-CoV-2 D614G S (**Fig. 1F**). Moreover, S2P6 inhibited SARS-
147 CoV S, Pangolin Guangdong 2019 (PANG-GD) S, MERS-CoV S and OC43 S VSV pseudotypes
148 with IC50 values ranging from 0.02 to 17 µg/ml (**Fig. 1G**). S2P6 therefore features an
149 unprecedented broad β-coronavirus neutralizing activity, including SARS-CoV-2 and SARS-CoV
150 sarbecovirus clades as well as members of the merbecovirus and embecovirus subgenera.
151   To define the epitopes recognized by the identified mAbs, we performed peptide mapping
152 experiments using 15-mer linear overlapping peptides (**fig. S2A**). All five mAbs bound to peptides
153 containing the SARS-CoV-2 motif F_{1148}KEELDKYF$_{1156}$ (**Fig. 1H**) located in the stem helix within
154 the S_2 subunit. This region is strictly conserved in SARS-CoV, highly conserved among other β-
155 coronaviruses, and overlaps with the epitopes of B6 (**Fig. 1I**) and 28D9, two mAbs which were
156 previously identified following mouse immunization (*12, 13*). S2P6 bound efficiently to the stem
157 helix peptides of the five β-coronaviruses that infect humans (albeit with a faster off-rate for HKU1)
158 as well as of the MERS-CoV-related bat viruses (HKU4 and HKU5) and murine hepatitis virus
159 (MHV) (**Fig. 1J** and **fig. S2B**). S2S43 exhibited similar overall binding to S2P6 with markedly
160 weaker reactivity towards the HKU1, HKU4 and HKU5 peptides, whereas the three clonally
161 related P34D10, P34G12, and P34E3 mAbs exhibited weaker or no binding to HKU4 and HKU5
162 peptides (**fig. S2B**).
163
164
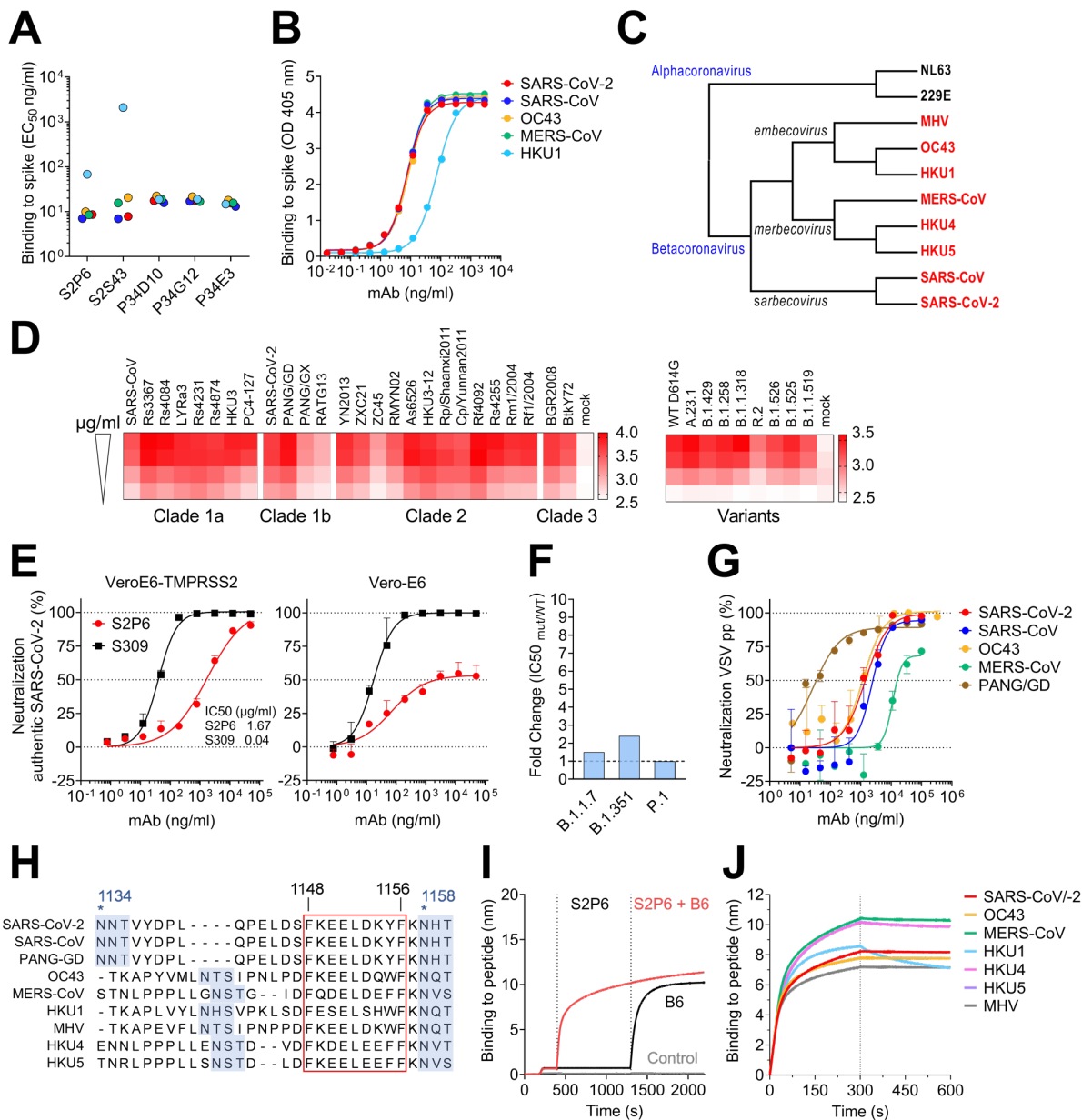
Fig. 1. The S2P6 cross-reactive mAb broadly neutralizes β-coronaviruses from three subgenera. (**A-B**) Binding avidity (EC50) of 5 mAbs to prefusion coronavirus S trimer ectodomains as determined by ELISA (A). S2P6 binding curves from one representative experiment out of two is shown (B). (**C**) Cladogram of representative α- and β-coronavirus S glycoprotein amino acid sequences inferred via maximum likelihood analysis. β-coronaviruses are highlighted in red. (**D**) Flow cytometry analysis of S2P6 binding (from 10 to 0.22 μg/ml) to a panel of 26 S glycoproteins representative of all *sarbecovirus* clades (left) and 8 SARS-CoV-2

174   variants (right) displayed as a heat map of log MFI (mean fluorescent intensity). (**E**) Neutralization
175   of authentic SARS-CoV-2 by S2P6 determined using VeroE6-TMPRSS2 (left) or Vero-E6 (right)
176   cells. S309 mAb that binds RBD site IV (*21*) is included for comparison. Mean ± s.d. of triplicates
177   from one representative experiment out of three is shown. (**F**) S2P6-mediated neutralization of
178   SARS-CoV-2 B.1.1.7 S, B.1.351 S and P.1 S VSV pseudotypes represented as IC50 fold change
179   relative to wildtype (D614G) S VSV pseudotype. (**G**) S2P6-mediated neutralization of VSV
180   pseudotyped with various β-coronavirus S glycoproteins. Error bars indicate standard deviation
181   of triplicates. IC50 values: 2.4 µg/ml, 1.4 µg/ml, 17.1 µg/ml, 1.3 µg/ml and 0.02 µg/ml for SARS-
182   CoV, SARS-CoV-2, MERS-CoV, OC43 and PANG/GD, respectively. (**H**) Alignment of β-
183   coronavirus stem helix region with the S2P6 epitope boxed. Residue numbering is shown
184   according to SARS-CoV-2 S. N-linked glycosylation sequons are highlighted in blue. (**I**)
185   Competition assay of S2P6/B6 binding to the identical stem helix peptide from SARS-CoV-2 and
186   SARS-CoV (herein defined as SARS-CoV/-2). B6 binding in presence of S2P6 (red line), B6
187   binding in absence of S2P6 (black line) and the no SARS-CoV/-2 stem peptide control (grey line)
188   is shown. (**J**) Kinetics of S2P6 binding to a panel of biotinylated β-coronavirus stem helix peptides
189   immobilized at the surface of biolayer interferometry biosensors.

190

191   **Structural basis for S2P6 binding to the conserved S glycoprotein stem helix**
192   To unveil the molecular basis of the exceptional S2P6 neutralization breadth, we
193   determined a cryo-EM structure of the SARS-CoV-2 S ectodomain trimer in complex with the Fab
194   fragments of S2P6 and S2M11 (to lock the RBDs in the closed state (*22*)) at 4.1 Å overall
195   resolution. The marked conformational dynamics of the region recognized by S2P6 limited the
196   local resolution of the stem helix/Fab to approximately ~12 Å (**Fig. 2A**, **table S1** and **fig S3**). 3D
197   classification of the cryo-EM data revealed incomplete Fab saturation (**fig. S3**). Our cryo-EM
198   structure confirms that S2P6 recognizes the stem helix and suggests that the mAb disrupts its
199   quaternary structure, which is presumed to form a 3-helix bundle in prefusion SARS-CoV-2 S (*3*,
200   *4, 12*). To overcome the limited resolution of the stem helix/Fab interface in the cryoEM structure,
201   we determined a crystal structure of the S2P6 Fab in complex with the SARS-CoV-2 S stem helix
202   peptide (residues 1146-1159) at 2.67 Å resolution (**Fig. 2B-D**, **fig. S4A** and **table S2**). The peptide
203   folds as an amphipathic α-helix resolved for residues 1146 to 1159. S2P6 buries approximately
204   600 Å^2 upon binding to its epitope using shape-complementarity and hydrogen bonding involving
205   complementarity determining regions (CDR) H1-H3, L1 and L3. The light chain residues Y33,
206   Y92, G93, P96, P97 and F99 as well as heavy chain residues Y33, I50, H57, T58, S59, P101,
207   K102 and G103 form a deep groove in which the hydrophobic side of the stem helix docks via
208   residues F1148, L1152, Y1155 and F1156. Binding specificity is provided through backbone
209   hydrogen bonding of residues F1148$_{SARS-CoV-2}$ and K1149$_{SARS-CoV-2}$ with CDRH3 P101, side chain
210   hydrogen bonding of residues E1151$_{SARS-CoV-2}$ with CDRL1 Y33 and CDRL3 S94, D1153$_{SARS-CoV-2}$
211   with CDRH1 Y33 side chains as well as Y1155$_{SARS-CoV-2\ S}$ with CDRH2 S59 through a water
212   molecule (**Fig. 2C-D**). The contribution of each epitope residue was validated by single
213   substitution scan analysis with most mutations at positions 1148, 1151-1153 and 1155-1156
214   abolishing S2P6 binding, highlighting the importance of these residues for binding (**fig. S5A**). A
215   substitution scan analysis performed on the P34D10, P34G12 and P34E3 mAbs revealed a
216   similar pattern of key interacting residues (**fig. S5A**). Residue Y1155 is conservatively substituted
217   to F1238$_{MERS-CoV}$ or W1237/1240$_{HKU1/OC43}$ and residue D1153 is conserved in MERS-CoV and

218 OC43 but mutated to S1235 for HKU1 (**fig. S5B**). The residue scan and structural results suggest
219 that the reduced binding affinity of S2P6 for HKU1 S is (at least partially) due to the $D1153_{SARS-CoV-2}S1235_{HKU1}$ substitution which is expected to abrogate or dampen electrostatic interactions
221 with the CDRH1 Y33 side chain hydroxyl (**Fig. 2C-D**).

222   Although S2P6 and B6 recognize a similar epitope (**fig. S4B-C**), they bind with opposite
223 orientations of the heavy and light chains relative to the stem helix and the S2P6-bound structure
224 resolves 3 additional C-terminal peptide residues (1156-1159) compared to the B6-bound
225 structure (1147-1156) (**fig. S4B-C**). Superposition of both structures based on the stem helix
226 reveals that B6 CDRH2 would sterically clash with $H1159_{SARS-CoV-2}$, putatively explaining the
227 broader cross-reactivity of S2P6 over B6 (**fig. S4B-C**).

228   To further validate our structural data, we carried out viral escape mutant selection in vitro
229 in the presence of S2P6 using a replication-competent VSV-SARS-CoV-2 S chimeric virus (*23*).
230 After two passages, virus neutralization by S2P6 was abrogated and deep sequencing revealed
231 the emergence of five distinct resistance mutations: L1152F, D1153N/G/A and F1156L, which are
232 consistent with the structural data and substitution scan analysis (**fig. S5A**). These mutations
233 have been detected with very low frequency in circulating SARS-CoV-2 isolates (146 out of
234 1,217,814 sequences as of April 30, 2021). The isolation of escape mutants in a VSV-SARS-CoV-
235 2 S chimeric virus system contrasts with the high conservation of the stem helix and suggest that
236 a selection pressure not recapitulated here could limit accumulation of mutations in this epitope
237 in the authentic virus.

238
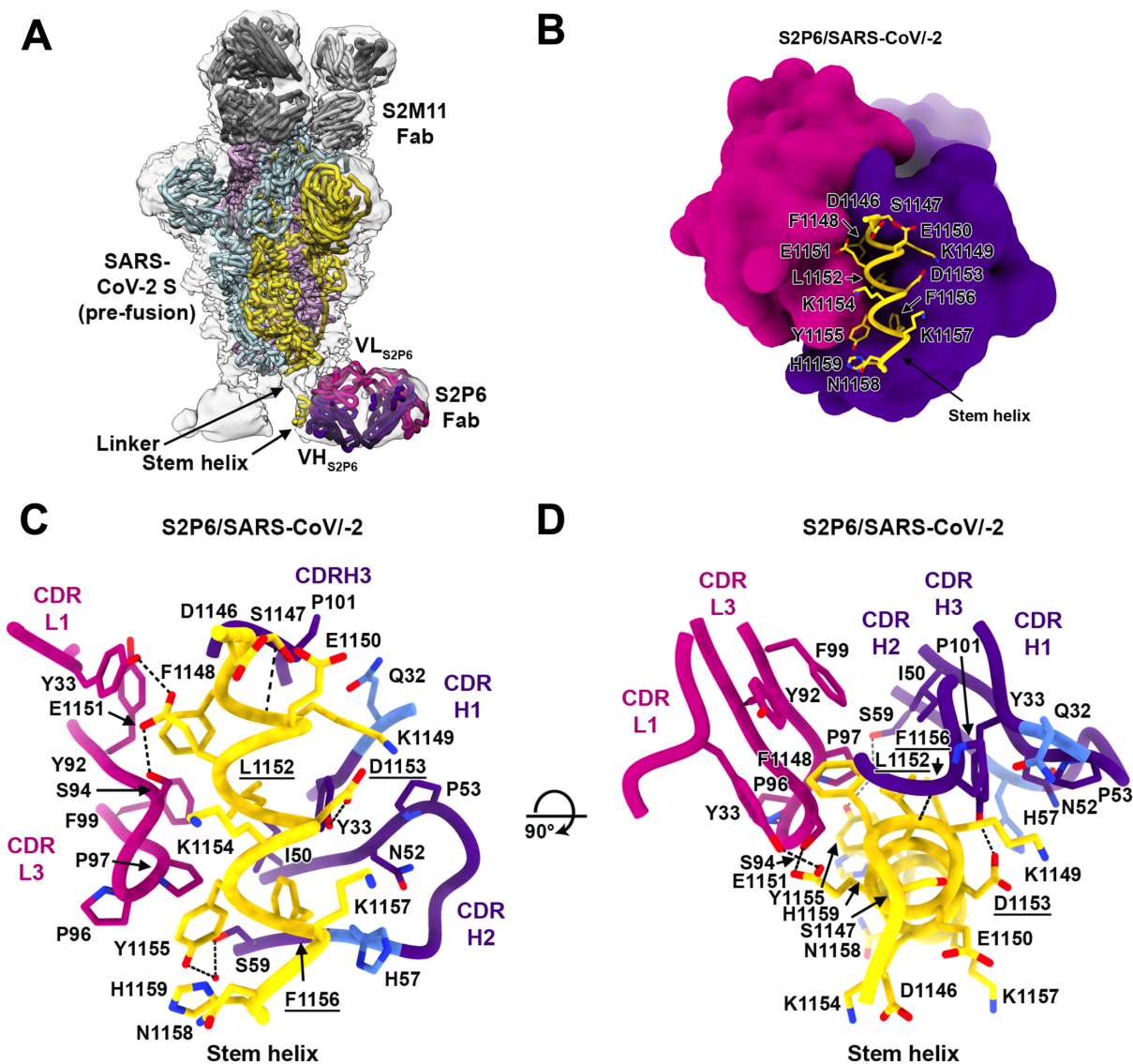
Fig. 2: Structural basis for the broad S2P6 cross-reactivity with a conserved coronavirus stem helix peptide. (**A**) Composite model of the S2P6-bound SARS-CoV-2 S cryoEM structure and of the S2P6-bound stem helix peptide crystal structure docked in the cryoEM map (transparent gray surface). SARS-CoV-2 S protomers are colored pink, cyan and gold, the S2P6 Fab heavy and light chains are colored purple and magenta and the S2M11 Fab heavy and light chains are colored dark and light gray, respectively. (**B**) Ribbon diagram of the S2P6 Fab (surface rendering) in complex with the SARS-CoV-2 S stem helix peptide (yellow ribbon with side chains rendered as sticks and labeled). (**C-D**) Ribbon diagram in two orthogonal orientations of the S2P6 Fab bound to the SARS-CoV-2 S stem helix peptide showing a conserved network of interactions. Only key interface residues and the S2P6 CDR loops are shown for clarity. Residues Q32 and H57, that are mutated during affinity maturation of the S2P6 heavy chain, are colored blue. Hydrogen bonds are indicated with dashed lines. Residues substituted in the escape mutants isolated are underlined.

254

**Stem helix-targeting mAbs inhibit S-mediated membrane fusion**

The S stem helix forms a 3-helix bundle in many prefusion cryoEM structures of SARS-CoV-2 S and SARS-CoV S (*3*, *4*, *11*, *24–26*). In contrast, the S2P6/S2M11/SARS-CoV-2 S cryoEM structure suggests that the quaternary organization of the stem is disrupted (**Fig. 2A**) as supported by the observation that S2P6 binds to the hydrophobic face of the stem helix which is expected to be mostly buried through homo-oligomeric interactions in prefusion S, and that may be only transiently available for Ab binding. Although we observed S2P6 binding to post-fusion SARS-CoV-2 S (**fig. S1C**), the epitope recognized is buried at the interface with the other two protomers of the rod-shaped trimer and is therefore not expected to be fully accessible (**fig. S4D**) (*12*, *27–29*). Based on these data, we hypothesized that S2P6 binding to S sterically interferes with the conformational changes leading to membrane fusion, as observed for B6 (*12*) and 27D9 (*13*).

To validate the inferred mechanism of S2P6-mediated broad coronavirus neutralization, we first showed that S2P6 binding did not block engagement of SARS-CoV-2 S by ACE2 using ELISA, as expected based on the remote location of its epitope from the RBD (**Fig. 3A**). S2P6, however, blocked cell-cell fusion between Vero-E6 cells transfected with full-length SARS-CoV-2 S as effectively as the S2M11 mAb which locks SARS-CoV-2 S in the closed state (*22*) (**Fig. 3B**). We previously described mAbs targeting RBD antigenic site Ia (e.g. S2E12) and IIa (e.g. S2X259 or S2X35) which can mimic receptor attachment and prematurely trigger fusogenic S conformational changes (*11*, *30*, *31*). Accordingly, S2P6 at concentrations as low as 1 ng/ml abrogated the formation of syncytia mediated by S2E12 (*30*). Collectively, these results suggest that the main mechanism of S2P6 neutralization is to prevent viral entry via inhibition of membrane fusion resulting from impeding S fusogenic rearrangements (**Fig. 3C**).

278
279
280
281
282
283
284
285
286
287
288
289
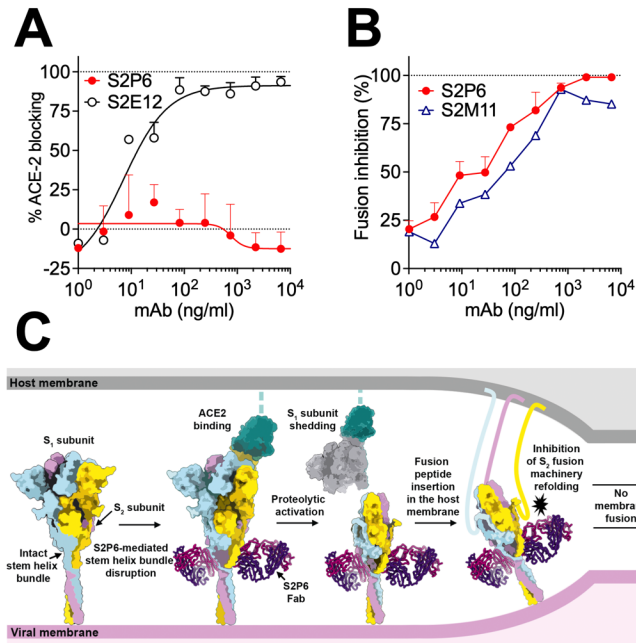
Fig. 3. S2P6 binding disrupts the stem helix bundle and sterically inhibits membrane fusion. (**A**) SARS-CoV-2 S binding to ACE2 in the presence of mAb S2P6 analyzed by ELISA. S2E12 was included as a positive control. (**B**) S2P6 inhibition of cell-cell fusion using Vero-E6 cells transfected with SARS-CoV-2 S. S2M11 was included as a positive control. Inhibition of fusion values are normalized to the percentage of fusion without mAb (100%) and to that of fusion of non-transfected cells (0%). (**C**) Proposed mechanism of inhibition mediated by the S2P6 mAb. S2P6 binds to the hydrophobic core of the stem helix bundle and disrupts its quaternary structure. S2P6 binding likely prevents S_2 subunit refolding from the pre- to the post-fusion state and blocks viral entry.

S2P6-mediated protection is enhanced by Fc-mediated effector functions in hamsters

Fc-mediated effector functions can contribute to in vivo protection by promoting viral clearance and anti-viral immune responses (*32–35*). We analyzed the ability of S2P6 to trigger activation of FcγRIIa and FcγRIIIa, as well as to exert Fc effector functions in vitro. S2P6 promoted moderate dose-dependent FcγRIIa and FcγRIIIa mediated signaling using a luciferase reporter assay (**Fig. 4A**). S2P6 promoted robust activation of Ab-dependent cell cytotoxicity (ADCC), to levels comparable to those observed with the S309 mAb (*21*), following incubation of SARS-CoV-2 S expressing CHO-K1 target cells with human peripheral blood mononuclear cells (PBMCs) (**Fig. 4B**). S2P6 also triggered Ab-dependent cellular phagocytosis (ADCP) activity using Cell-Trace-Violet-labelled PBMCs as phagocytic cells, and SARS-CoV-2 S expressing CHO (CHO-S) as target cells (**Fig. 4C**). Finally, S2P6 did not promote complement-dependent cytotoxicity (CDC) (**Fig. 4D**) indicating that S2P6 Fc-mediated effector functions, but not complement activation, might participate in viral control in vivo.

We next evaluated the prophylactic activity of S2P6 against challenge with the prototypic (Wuhan-1 related) SARS-CoV-2 in a Syrian hamster model (*36*). As we previously showed that human IgG1s poorly recognize FcγRs (*30*), we compared S2P6 harboring a human IgG1 (Hu-S2P6) or a hamster IgG2a constant region (Hm-S2P6), the latter enabling optimal interactions with hamster FcγRs. Two different doses of Hu-S2P6 or Hm-S2P6 were administered 24 hours prior to intranasal SARS-CoV-2 challenge and the lungs of the animals were assessed 4 days post-infection for viral RNA load and replicating virus. Hm-S2P6 administered at 20 mg/kg reduced viral RNA copies and replicating viral titers in the lungs of animals by two orders of magnitude relative to a control mAb (**Fig. 4E**). Moreover, Hm-S2P6 at 20 mg/kg reduced viral RNA copies detected in the lungs to levels significantly lower than those observed with Hu-S2P6, suggesting a beneficial effect of S2P6 effector functions in vivo. Based on the comparable S2P6 neutralization potencies towards SARS-CoV-2 VOC observed in vitro (**Fig. 1F**), we set out to assess the protective efficacy of S2P6 in hamsters challenged with SARS-CoV-2 B.1.351. Prophylactic administration of Hu-S2P6 at 20 mg/kg reduced replicating viral titers in the lungs (but not RNA copy numbers) by ~1.5 order of magnitude relative to the control group, in line with the strict conservation of the stem helix epitope in all VOC identified to date (**Fig 4F**).

Collectively, these findings demonstrate that Abs targeting a highly conserved epitope in the S fusion machinery can trigger Fc-mediated ADCC and ADCP in vitro and protect against SARS-CoV-2 challenge by leveraging both neutralization and effector functions in vivo.
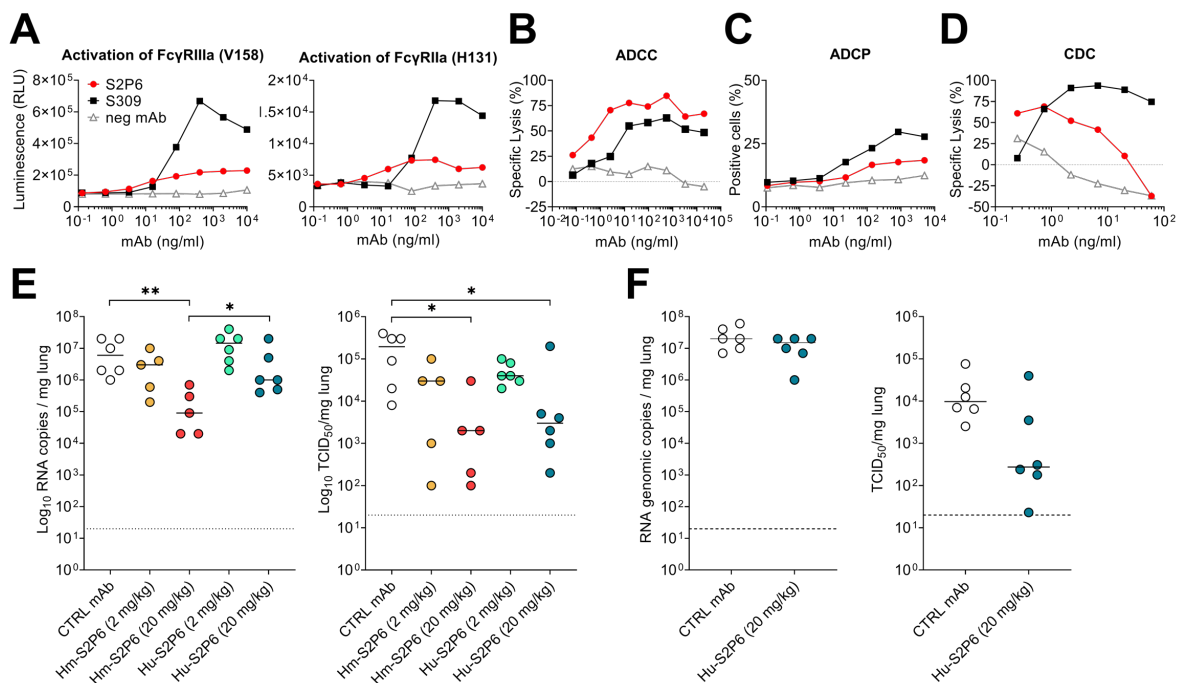
Fig. 4. S2P6 activates effector functions and protects Syrian hamsters from SARS-CoV-2 challenge. (A) NFAT-driven luciferase signal induced in Jurkat cells stably expressing FcγRIIIa (V158, left) or FcγRIIa (V131, right) upon S2P6 binding to full-length wild-type SARS-CoV-2 S expressed at the surface of CHO target cells. S309 is included as positive control. RLU, relative luminescence unit. (**B**) mAb-mediated ADCC using SARS-CoV-2 CHO-K1 cells (genetically engineered to stably express a HaloTag-HiBit-tagged) as target cells and PBMC as effector cells. The magnitude of NK cell–mediated killing is expressed as percentage of specific lysis. (**C**) mAb-mediated ADCP using Cell-Trace-Violet-labelled PBMCs as a source of phagocytic cells (monocytes) and PKH67–fluorescently labeled S-expressing CHO cells as target cells. The *y*-axis indicates percentage of monocytes double-positive for anti-CD14 (monocyte) marker and PKH67. (**D**) Lysis of SARS-CoV-2 S stably transfected CHO cells by mAbs in the presence of complement (CDC assay). (**E**) Syrian hamsters were administered with the indicated amount of S2P6 mAb harboring either a hamster (Hm-S2P6) or a human (Hu-S2P6) constant region before intranasal challenge with prototypic SARS-CoV-2 (Wuhan-1 related). An irrelevant mAb (MGH2 against CSP of *P. falciparum*) at 20 mg/kg was used as negative control (*37*). Shown are viral RNA loads (left) and replicating virus titers (right). (**F**) Prophylactic administration of 20 mg/kg of human S2P6 in hamsters challenged with SARS-CoV-2 B.1.351 VOC. Shown are viral RNA loads (left) and replicating virus titers (right). ∗ P<0.05, ∗∗ P<0.01 Mann-Whitney test.

Natural infection or vaccination predominantly elicit stem helix-directed Abs of narrow specificities

To understand how frequently stem helix-specific Abs are elicited, we performed serological analysis using plasma samples from pre-pandemic, COVID-19 convalescent, and COVID-19 vaccinated individuals (**Fig. 5A** and **fig. S6**). We determined the titers of plasma IgG binding to stem helix peptides of SARS-CoV-2/SARS-CoV (SARS-CoV/-2), OC43, MERS-CoV, HKU1, HKU4 and HKU5. We did not observe plasma Abs binding to stem helix peptides in pre-pandemic samples, except for HKU1, probably reflecting prior infection with this virus in this cohort. Conversely, stem helix-specific Abs were found at low frequency in individuals previously infected with SARS-CoV-2 or receiving two doses of mRNA vaccines (**Fig. 5A**). Overall, these data show that plasma Ab responses to the stem helix are elicited upon SARS-CoV-2 infection or vaccination although they are relatively rare.

Next, we investigated the frequency of stem helix specific Abs in the memory B cell repertoire of 21 convalescent and 17 vaccinated individuals using a clonal analysis based on in vitro polyclonal stimulation (*38*), here referred as antigen-specific B-cell memory repertoire analysis (AMBRA) (**Fig. 5B-G** and **fig. S6-S8**). In both cohorts, we observed frequencies of stem helix specific IgGs ranging from 0.1-2.5%, except for one individual (infected and vaccinated with a single dose of mRNA vaccine) for whom we measured an exceptionally high frequency of SARS-CoV/-2 stem helix-specific Abs (**fig. S8**). Most SARS-CoV-2 stem helix specific Abs were found to be cross-reactive with OC43, consistent with the high sequence identity of the stem helices of these two viruses (**Fig. 1H**). Abs specific for the HKU1 S stem helix were found in some individuals but they were not cross-reactive with other β-coronaviruses (**Fig. 5D** and **G**). This analysis revealed a single example of cross-reactivity to all stem helix β-coronavirus peptides tested (**Fig. 5E**), whereas most others Abs show a more limited cross-reactivity among β-coronaviruses.

Broadly reactive β−coronavirus Abs acquire affinity and breadth through somatic mutations

To define the ontogeny of the broadly reactive β−coronavirus mAbs described here, we generated a panel of germline variants of S2P6, P34D10, P34E3 and P34G12 mAbs. Two out of seven S2P6 heavy chain residues that are mutated relative to germline contribute to epitope recognition (Q32 and H57) whereas none of the 5 light chain mutated residues participate in S binding (**Fig. 2C-D**). To address the role of VH and VK somatic mutations we therefore generated a panel of S2P6 germline variants for the heavy or the light chain, or both variable regions (VH and VK). The fully germline S2P6 (UCA) bound to OC43 and MERS-CoV stem helix peptides (with approximately 1 order of magnitude higher EC50 compared to the mutated mAb) but not to SARS-CoV/-2 or HKU1 peptides (**Fig. 5H**). Somatic mutations in VH were sufficient for high avidity binding to SARS-CoV/-2, whereas both VH and VK mutations were required for optimal binding to HKU1. The presence of residue G103 in CDRH3 was found to be essential for binding to all β-coronaviruses (**fig. S9A**). Collectively, these findings indicate that the S2P6 mAb likely arose in response to OC43 infection, and its specificity was broadened towards SARS-CoV-2 and HKU1 through somatic mutations selected upon natural infection with one or both of these β-coronaviruses. In contrast, analysis of UCA binding of the clonally related P34D10, P34G12 and P34E3 mAbs suggest they were likely primed by HKU1 infection, rather than OC43, and acquired

405   breadth towards the other human β-coronaviruses primarily through somatic mutations in VH (**Fig.**
406   **5I** and **fig. S9B**). Together with the serological and B cell repertoire analysis, these findings
407   demonstrate that broadly reactive β-coronavirus Abs may result from priming of virus-specific B
408   cells gaining affinity and breadth through somatic mutations in response to heterotypic
409   coronavirus exposures.
410

411
412
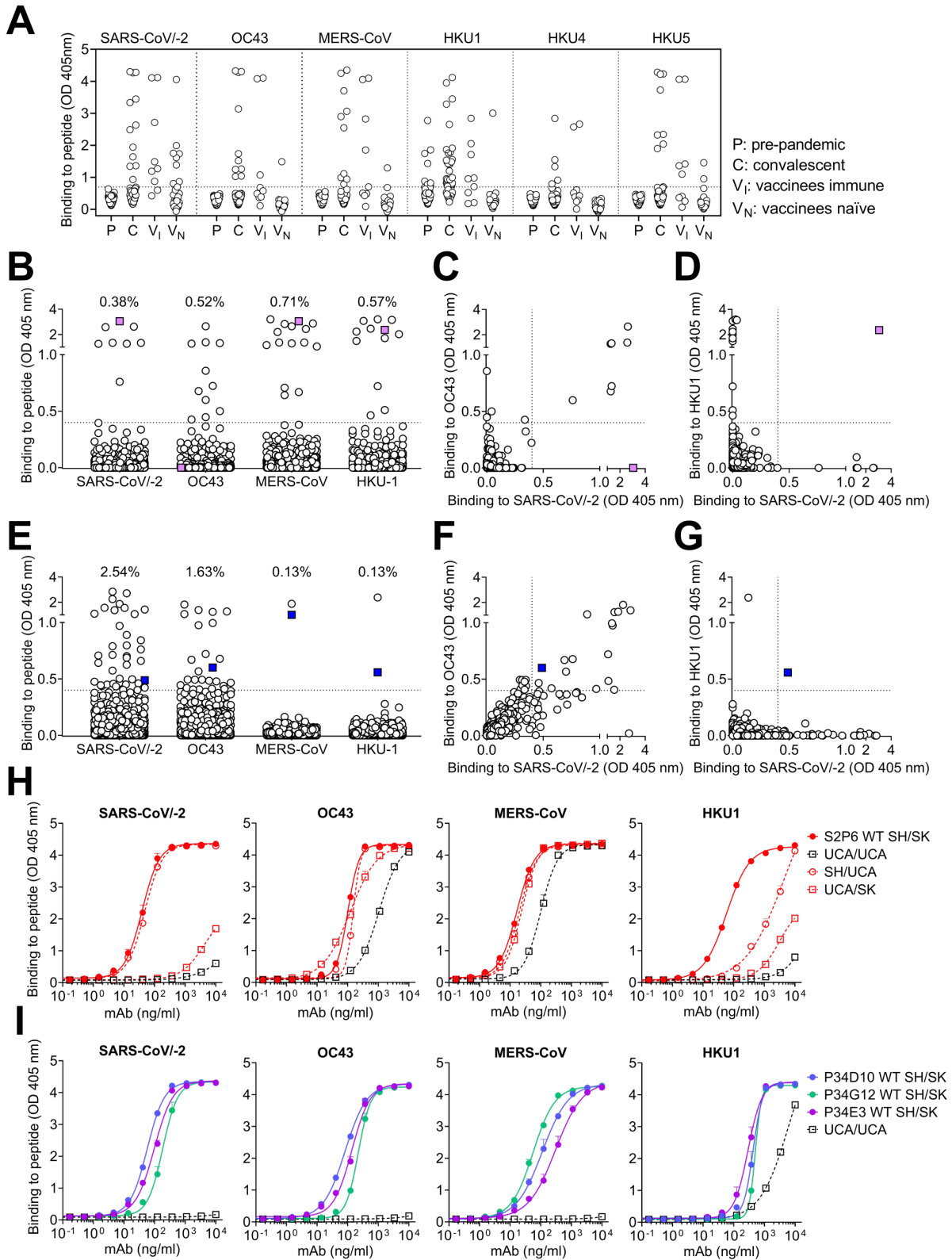
Fig. 5: Stem helix-directed Abs are of narrow specificities and acquire affinity and breadth through somatic mutations. (**A**) Binding of pre-pandemic (P, n=88), COVID-19 convalescent (C, n=72), vaccinees immune (VI, n=9) and vaccinees naïve (VN, n=37) plasma Abs diluted 1:10 to β-coronavirus stem helix peptides analyzed by ELISA. A cut-off of 0.7 was determined based on signal of pre-pandemic samples and binding to uncoated ELISA plates. (**B-G**) Analysis of memory B-cell binding to β-coronavirus stem helix peptides from 21 COVID-19 convalescent individuals (B-D) and 16 vaccinees (E-G). Each dot representing individual culture containing oligo-clonal B cells screened against stem helix peptides in ELISA. Pairwise reactivity comparison is shown for SARS-CoV/-2 and OC43 (C and F) and SARS-CoV/-2 and HKU1 (D and G). Highlighted in color are cultures cross-reactive with at least three peptides. (**H-I**) Binding of S2P6 (H) (mutated SH/SK), fully germline reverted (UCA/UCA), germline reverted heavy chain paired with mature light chain (UCA/SK), mature heavy chain paired with germline reverted light chain (SH/UCA) and of P34D10, P34G12 and P34E3 (I) (WT SH/SK), and germline reverted (UCA/UCA) to stem helix peptides.

Discussion

The coronavirus S_2 subunit (fusion machinery) contains several important antigenic sites, including the fusion peptide and the heptad-repeat 2 regions, and is more conserved than the S_1 subunit (*39–43*). As a result, it is an attractive target for broad coronavirus detection and neutralization (*44*). The recent identification of 4 cross-reactive mAbs targeting the stem helix unveiled this previously unknown S_2 subunit epitope, which is conserved among β-coronavirus S glycoproteins (*12–14*, *45*), although none of them inhibit members of all three β-coronavirus subgenera (lineages). Here, we identified five mAbs targeting overlapping epitopes in the S stem helix and cross-reacting with human and animal β-coronaviruses. We showed that S2P6 broadly neutralizes all sarbecoviruses, merbecoviruses and embecoviruses evaluated through inhibition of membrane fusion. The exceptionally broad cross-reactivity and neutralization breadth of S2P6 is explained by the conserved nature of the stem helix among β-coronaviruses. Fewer than ~0.06% SARS-CoV-2 sequences have been reported to be mutated between S residues 1146 and 1159 out of more than 1.3 million genomes deposited in GISAID as of April 2021 and no SARS-CoV-2 VOC harbor residue substitutions within this region.

We also provide evidence that a S_2 subunit-directed mAb protects hamsters from SARS-CoV-2 challenge, including with the SARS-CoV-2 B.1.351 VOC, with a beneficial effect of Fc-mediated effector functions. These data extend previous studies describing the participation of effector functions to in vivo efficacy of SARS-CoV-2 RBD-specific mAbs (*32, 35*) as well as influenza A hemagglutinin stem-specific broadly neutralizing mAbs (*46, 47*). These observations is reminiscent of similar findings for mAbs targeting a highly conserved epitope on the influenza virus hemagglutinin stem, and indicate that the combination of mAb cross reactivity with effector functions may provide particular potency against these viruses (*15*).

The stem helix is presumed to form a 3-helix bundle in prefusion SARS-CoV-2 S and dynamic conformational changes are likely required to expose the otherwise buried hydrophobic epitope, which is surrounded by conserved glycans potentially further shielding this conserved site. We provide evidence that stem helix-targeted Abs are elicited upon natural infection by endemic (OC43 or HKU1) or pandemic (SARS-CoV-2) coronaviruses as well as by COVID-19 mRNA vaccines. However, stem helix-specific Abs are present at low titers in plasma samples of

457   convalescent or vaccinated individuals and at low frequency in their memory B cell repertoire
458   possibly as a result of limited epitope exposure, similarly to the sub-dominance of Abs to the
459   conserved hemagglutinin stem region of influenza A viruses (*46*, *48*).

460   Stem helix-targeted Abs are predominantly of narrow specificities and only few of them
461   mediate broad β-coronavirus neutralization and protection through accumulation of somatic
462   mutations. These findings along with the moderate neutralization potency and low frequency of
463   such mAbs in COVID-19 convalescent or vaccinated subjects indicate that eliciting high enough
464   titers of stem helix-targeted mAbs through vaccination will be a key challenge to overcome to
465   develop pan-β-coronavirus vaccines. We propose that harnessing recent advances in
466   computational protein design, such as epitope-focused vaccine design approaches (*49–51*) and
467   multivalent display (*52–57*), to target the stem helix or the fusion peptide regions might prove
468   necessary to elicit broad β-coronavirus immunity.

469

470

494

Author contributions
495
496 Experiment design: D.P., M.M.S., J.S.L., M.A.T., M.S.P., H.W.V, MB., D.C., D.V. Donors'
497 Recruitment and Sample Collection: E.C., F.B., B.G., A.C., P.F., P.E.C., O.G., S.C., C.G., A.R.,
498 L.P., M.S., D.V., C.H.D. Antibody discovery: D.P., MB., J.S.L., J.J., S.J., N.S., K.C., E.C., D.C.
499 AMBRA preparation: C.S.F., J.B., A.C. Expression and purification of proteins: A.C.W., J.E.B.,
500 J.J. Antibody functional experiments: D.P., M.M.S., N.C., J.S.L., M.A.T., A.C.W., F.L., J.N., S.B.,
501 R.M. Bioinformatic analysis of virus diversity and variants: J.d.I., I.B., A.T. Evaluation of effector
502 functions: B.G. SPR Binding Assays: L.E.R. Neutralization assay: D.P., M.A.T., F.A.L., J.N., M.
503 P. H. Escape mutants selection and sequencing: H.K., S.I., F.A.L., J.d.I. Effects in the hamster
504 model and data analysis: R.A., C.F., C.D.K., L.B, L..C, J.N., E.V., F.B. Cryo-EM Data Collection,
505 Processing, and Model Building, M.M.S., D.V. Crystallization, X-Ray Crystallography Data
506 Collection, Processing, and Model Building: M.M.S., N.C., G.S., D.V. Serological Assays: D.P.,
507 R.M. Data Analysis: D.P., M.M.S., M.B., J.S.L., J.J., F.A.L., J.N., N.C., A.M.T., A.C.W., G.S., D.C.,
508 D.V. Manuscript Writing: D.O.P., M.M.S., J.S.L., M.B., G.S., F.S., A.L., H.W.V, D.C., D.V.

509

515   disclose the subject matter described in this manuscript. D.V. is a consultant for Vir Biotechnology
516   Inc. The Veesler laboratory and the Sallusto laboratory have received sponsored research
517   agreements from Vir Biotechnology Inc. The other authors declare no competing interests.
518
519

520   **Materials and Methods**

521

522   **Cell lines**
523   Cell lines used in this study were obtained from ATCC (HEK293T and Vero-E6) or ThermoFisher
524   Scientific (ExpiCHO cells, FreeStyle™ 293-F cells and Expi293F™ cells).

525

526   **Sample donors**
527   Samples were obtained from cohorts of individuals enrolled before June 2019 (pre-pandemic), of
528   SARS-CoV-2 infected individuals or of vaccinated individuals immunized with Moderna or
529   Pfizer/BioNTech BNT162b2 vaccines under study protocols approved by the local Institutional
530   Review Boards (Canton Ticino Ethics Committee, Switzerland, the Ethical committee of Luigi
531   Sacco Hospital, Milan, Italy and WCG North America, Princeton, NJ, US). All donors provided
532   written informed consent for the use of blood and blood components (such as human peripheral
533   blood mononuclear cells (PBMCs), sera or plasma) and were recruited at hospitals or as
534   outpatients. PBMCs were isolated from blood by Ficoll density gradient centrifugation and either
535   used freshly or stored in liquid nitrogen for later use. Sera were obtained from blood collected
536   using tubes containing clot activator, followed by centrifugation and stored at -80°C.

537

538   **AMBRA (antigen-specific memory B cell repertoire analysis) of IgG antibodies**
539   Replicate cultures of total unfractionated PBMC from SARS-CoV-2 infected or vaccinated
540   individuals were seeded in 96 U-bottom plates (Corning) in RPMI1640 supplemented with 10%
541   Hyclone, sodium pyruvate, MEM non-essential amino acid, stable glutamine and Penicillin-
542   Streptomycin. Memory B cell stimulation and differentiation was induced by adding 2.5 µg/ml
543   R848 (3 M) and 1000 U/ ml human recombinant IL-2 for 10 days at 37 °C 5% CO_2. The cell culture
544   supernatants were collected for further analysis.

545

546   **Antibody discovery and expression**
547   Antigen specific IgG$^+$ memory B cells were isolated and cloned from total PBMCs of convalescent
548   individuals. Abs VH and VL sequences were obtained by reverse transcription PCR (RT-PCR)
549   and mAbs were expressed as recombinant human IgG1, carrying the half-life extending
550   M428L/N434S (LS) mutation in the Fc region or Fab fragment. ExpiCHO cells were transiently
551   transfected with heavy and light chain expression vectors as previously described (*21*). For in vivo
552   experiments in Syrian hamsters, S2P6 was produced with a Syrian hamster IgG2 constant
553   region. Using the Database IMGT (http://www.imgt.org), the VH and VL gene family and the
554   number of somatic mutations were determined by analyzing the homology of the VH and VL
555   sequences to known human V, D and J genes. UCA sequences of the VH and VL were
556   constructed using IMGT/V-QUEST.
557   MAbs affinity purification was performed on ÄKTA Xpress FPLC (Cytiva) operated by UNICORN
558   software version 5.11 (Build 407) using HiTrap Protein A columns (Cytiva) for full length human

559 and hamster mAbs and CaptureSelect CH1-XL MiniChrom columns (ThermoFisher Scientific) for
560 Fab fragments, using PBS as mobile phase. Buffer exchange to the appropriate formulation buffer
561 was performed with a HiTrap Fast desalting column (Cytiva). The final products were sterilized
562 by filtration through 0.22 µm filters and stored at 4ºC.
563

Flow cytometry of antibody on S Protein expressing ExpiCHO-S cells
565 For Expi-CHO cell transient transfection, S plasmids (*21, 58*) were diluted in cold OptiPRO SFM,
566 mixed with ExpiFectamine CHO Reagent (Life Technologies, A29130) and added to the cells
567 seeded at 6×10^6 cells/ml in a volume of 5 ml in a 50 ml bioreactor. Transfected cells were
568 incubated at 37°C, 8% CO_2 with an orbital shaking speed of 209 rpm (orbital diameter of 25 mm)
569 for 42 hours. To test mAb binding, transfected ExpiCHO cells were collected, washed twice in
570 wash buffer (1% w/v solution of Bovine Serum Albumin (BSA; Sigma) in PBS, 2 mM EDTA) and
571 distributed at 60,000 cells/well into 96 U-bottom plates (Corning). mAb serial dilutions from 10
572 µg/ml were added onto cells for 30 minutes on ice and, after two washes, Alexa Fluor647-labelled
573 Goat Anti-Human IgG (Jackson Immunoresearch, 109-606-098) was used for detection. After 15
574 minutes of incubation on ice, cells were washed twice and mAb binding analyzed by flow
575 cytometry using a ZE5 Cell Analyzer (Biorard).
576

Protein expression and purification
578 SARS-CoV-2 S 2P, SARS-CoV S 2P, MERS-CoV S 2P, OC43 S, HKU1 S2P, and HKU4 S2P
579 ectodomains were produced as previously described (*3, 11, 12, 59, 60*). SARS-CoV-2 S D614G,
580 used for production of SARS-CoV-2 postfusion, contains a mu-phosphatase signal peptide
581 beginning at 14Q, a mutated S_1/S_2 cleavage site (SGAR), and ends at residue K1211 followed by
582 a TEV cleavage, foldon trimerization motif, and an 8X his tag in a pCMV vector. Briefly,
583 spike glycoproteins were produced in Expi293F cells grown in suspension using Expi293
584 expression medium (Life Technologies) at 37˚C in a humidified 8% CO_2 incubator rotating at 130
585 rpm. The cultures were transiently transfected using PEI with cells grown to a density of 3 million
586 cells per mL and cultivated for 3 days. The supernatant was clarified and affinity purified using a
587 1 mL HisTrapFF column (Cytiva). To isolate post-fusion SARS-CoV-2 S, SARS-CoV-2 S D614G
588 ectodomain was incubated for one hour with the S2X58 triggering Fab (*61*) and 1 µg/ml trypsin
589 before size-exclusion chromatography purification using a Superose 6 Increase 10/24 column
590 (Cytiva). Purified protein was concentrated, quantified using absorption at 280 nm, and flash
591 frozen in Tris-saline (20 mM Tris pH 8.0, 100 mM NaCl).
592
593

Enzyme-linked immunosorbent assay (ELISA)
595 96-well plates (Corning) were coated overnight at 4°C with recombinant proteins at 1 µg/ml or
596 peptides at 8 µg/ml diluted in phosphate-buffered saline (PBS). Plates were blocked with a 1%
597 w/v solution of Bovine Serum Albumin (BSA; Sigma) in PBS and serial dilutions of mAbs were
598 added for 1 hour at room temperature. When testing human plasma or memory B-cell
599 supernatants, plates were blocked with Blocker Casein (1% w/v) in PBS (Thermo Fisher
600 Scientific) supplemented with 0.05% Tween 20. Plasma and memory B-cell supernatants
601 (AMBRA testing) were then incubated for 1 hour at room temperature at a 1:10 and 1:2 dilution,
602 respectively. After further wash, mAbs bound were revealed using an anti-human IgG coupled to

603   alkaline phosphatase (Jackson Immunoresearch) incubated for 1 hour. Substrate (p-NPP, Sigma)
604   was used for color development and plates read at 405 nm by a microplate reader (Biotek). The
605   data were plotted with GraphPad Prism software.
606   For ELISA with plasma, cut-off value (OD=0.7) was determined based on signal of pre-pandemic
607   samples and binding to uncoated ELISA plates. For AMBRA, cut off value (OD= 0.4) was
608   determined as three times the mean OD values of negative wells.
609

610   **Blockade of SARS-CoV-2 S binding to ACE2**
611   SARS-CoV-2 S prefusion (final concentration 300 ng/ml) was incubated with 1 µg/ml of S309
612   mouse Fc-tagged mAb (S309-mFc) 30 minutes at 37°C before the addition of serially diluted S2P6
613   (from 20 µg/ml) and incubated for additional 30 minutes at 37°C. The complex S:S309:S2P6 was
614   then added to a pre-coated hACE2 (2 µg/ml in PBS) 96-well plate MaxiSorp (Nunc) and incubated
615   1 hour at room temperature. Subsequently, the plates were washed and a goat anti-mouse IgG
616   (Southern Biotech) coupled to alkaline phosphatase (Jackson Immunoresearch) added to detect
617   SARS-CoV-2 S:S309-mFc binding. After further washing, the substrate (p-NPP, Sigma) was
618   added, and plates read at 405 nm using a microplate reader (Biotek). The percentage of inhibition
619   was calculated as follow: (1-((OD sample-OD neg ctr)/(OD pos. ctr-OD neg. ctr))*100.
620

621   **Epitope identification and substitution scan**
622   PEPperMAP Epitope Mapping (PEPperPRINT GmbH, Heidelberg, Germany) was performed to
623   determine mAbs epitope through a pan-corona Spike protein Microarray covering the S proteins
624   of all β-coronaviruses. Briefly, microarray containing 15-mer peptides (overlapping of 13-mer) was
625   incubated with 10 µg/ml mAb for 16 hours at 4°C shaking at 140 rpm followed by staining with
626   Goat anti-human IgG (H+L) DyLight680 for 45 minutes at room temperature. Microarray read-out
627   was performed with a LI-COR Odyssey Imaging System at scanning intensities of 7/7 (red/green).
628   Epitope substitution scan was performed on the identified epitope based on a stepwise single
629   amino acid exchange on all amino acid positions. The mAbs binding to the generated microarray
630   was performed as above.
631

632   **Conservation analysis**
633   Conservation analysis was performed as described previously (Pinto et al 2020). SARS-CoV-2
634   S sequences were obtained from GISAID (https://www.gisaid.org/) on Apr 22nd 2021, the other
635   viruses sequences were obtained from NCBI Virus
636   (https://www.ncbi.nlm.nih.gov/labs/virus/vssi/#/) in December 2020. The multiple sequences
637   alignment was performed using MAFFT (https://mafft.cbrc.jp/alignment/software/) with the spike
638   amino acid sequences as input.
639

640   **SPR binding measurements**
641   SPR binding measurements were performed using a Biacore T200 instrument using anti-AviTag
642   pAb covalently immobilized on CM5 chips to capture S ECDs except the Cytiva Biotin CAPture
643   kit was used to capture biotinylated OC43 S ECD. Running buffer was Cytiva HBS-EP+ (pH 7.4)
644   or 20 mM phosphate pH 5.4, 150 mM NaCl, 0.05% P-20, for neutral or acidic pH experiments,
645   respectively. All measurements were performed at 25 °C. S2P6 Fab or IgG concentrations were
646   11, 33, 100, and 300 nM run as single-cycle kinetics. Double reference-subtracted data were fit
647   to a binding model using Biacore Evaluation software. All data for SARS-CoV-2 S, SARS-CoV S,

648   and OC43 S were fit to a 1:1 binding model. Data for MERS S were fit to a Heterogeneous Ligand
649   binding model, due to a kinetic phase with very slow dissociation presumed to be an artifact; the
650   lower affinity of the two KDs returned by the fit is reported as the KD of the S2P6:MERS S
651   interaction and is indicated to be approximate (the Rmax associated with the higher affinity kinetic
652   phase is proportional to the magnitude of the final signal above baseline). Data for HKU1 S were
653   fit to a steady-state binding model, because of the low signal and fast approach to equilibrium
654   within each association phase; the reported KD is indicated to be approximate. IgG binding data
655   yield an "apparent KD" due to avidity.
656

657   **Neutralization of authentic SARS-CoV-2 virus**
658   For SARS-CoV-2 neutralization experiments, cells were cultured in DMEM (Gibco 11995-040)
659   supplemented with 10% FBS (VWR 97068-085 lot#345K19) and 100 U/ml Penicillin-Streptomycin
660   (Gibco 15140-122). Cells were seeded in black, 96-well glass bottom plates (Cellvis P96-1.5H-N)
661   at a density of 20,000 cells/well. In a BSL3 facility, serial dilutions of mAbs (1:4) were incubated
662   with 200 PFU (plaque forming units, corresponding to a multiplicity of infection of 0.01) of authentic
663   SARS-CoV-2 (isolate USA-WA1/2020, passage 3, passaged in Vero-E6 cells) for 30 minutes at
664   37°C. After removal of cell culture supernatants, cells were infected with the virus:mAb mixtures
665   and incubated for 20 hours at 37°C. Cells were then fixed with 4% paraformaldehyde (Electron
666   Microscopy Sciences, 15714-S) in PBS (Gibco 10010-031) for 30 minutes, permeabilized with
667   0.1% Triton X-100 (Sigma, X100-500ML) for 30 minutes, and stained with Human SARS
668   Coronavirus Nucleoprotein/NP Ab, Rabbit Mab (Sino Biological, 40143-R001) at a dilution of
669   1:2000 dilution in 2% milk (RPI, M17200-500.0) for 1 hour. Subsequently, cells were stained with
670   Goat anti-Rabbit IgG (H+L) AF647 (Invitrogen, Cat. A21245 Lot. 223 2862) at a dilution of 1:1000
671   and 2 ug/ml Hoechst 33342 in 2% milk for 1 hour. Plates were imaged with an automated
672   microscope (Cytation5, Biotek), and nuclei and cells positive for the SARS-CoV-2 Nucleoprotein
673   were quantified using the supplied Gen5 software.
674

675   **VSV pseudotype virus production and neutralization**
676   Sarbecovirus spike cassettes with a C-terminal deletion of 19 amino acids (D19) were synthesized
677   and cloned into mammalian expression constructs (pcDNA3.1(+) or pTwist-CMV) for the following
678   Sarbecoviruses: SARS-CoV-2 (Accession QOU99296.1), SARS-CoV-1 (Accession
679   AAP13441.1), hCoV-19/pangolin/Guangdong/1/2019 (GD19, Accession QLR06867.1), and
680   Middle East respiratory syndrome-related coronavirus (MERS, Accession YP_009047204). To
681   generate pseudotyped VSV, 293T Lenti-X packaging cells (Takara, 632180) were seeded in 15
682   cm dishes such that the cells would be 80% confluent the following day. Cultures were then
683   transfected with various S expression plasmids using TransIT-Lenti transfection reagent (Mirus,
684   6600) according to the manufacturer's instructions. 24 hours after transfection, the packaging
685   cells were infected with VSV-G*ΔG-luciferase (Kerafast, EH1020-PM). 48 hours after infection
686   the supernatant containing Sarbecovirus pseudotyped VSV-luc was collected, centrifuged at 1000
687   × g for 5 minutes, aliquoted and frozen at −80°C.
688

689   To perform pseudotype neutralization assays, VeroE6-TMPRSS2 cells were used for VSV-SARS-
690   CoV-2, VSV-SARS-CoV-1, and VSV-GD19 and Huh7 cells were used for VSV-MERS. Cells were
691   seeded into clear bottom white-walled 96-well plates at 20,000 cells/well. The following day, 1:3

692   serial dilutions of Ab were prepared in DMEM and pseudotyped VSVs (final dilution 1:20) were
693   added to each mAb dilution and incubated for 1 hour at 37°C. Media was removed from the cells
694   and replaced with 50 µl of pseudotype:mAb complex and one hour post-infection, 50 µl of
695   complete culture media was added to the cells and incubated overnight at 37°C. The media from
696   infected cells was then removed and 100 µl of 1:1 diluted PBS:Bio-Glo (Promega, G7940)
697   luciferase substrate was added to each well. The plates were shaken at 300 rpm at room
698   temperature for 10 minutes and relative light units (RLUs) were then read on an EnSight
699   microplate reader (Perkin Elmer). Percent neutralization was determined by subtracting the mean
700   background (uninfected cells with luciferase substrate alone) values of 6 wells per plate from all
701   data points. Percent neutralization for each mAb concentration was calculated relative to control
702   wells receiving no mAb for each plate. Percent neutralization data were analyzed using GraphPad
703   Prism. Absolute IC_{50} values were calculated by fitting a curve using a variable slope 4 parameter
704   non-linear regression model and values were interpolated from the curve at y=50.
705

706   Production of OC43 S (AAT84354.1) pseudotyped VSV virus and neutralization assays was
707   performed similarly to previously described (12). Briefly, HEK-293T cells at 70~80% confluency
708   were transfected with the pCDNA3.1 expression vectors encoding full-length OC43 S harboring
709   a truncation of the 17 C-terminal residues along with a fusion to Ha-tag and the bovine coronavirus
710   hemagglutinin esterase protein Fc-tagged at molar ratios of 7:1. The day after, cells were
711   transduced with VSVΔG/Fluc (20). After 2 h, infected cells were washed four times with DMEM
712   before adding medium supplemented with anti-VSV-G antibody (I1- mouse hybridoma
713   supernatant diluted 1 to 25, from CRL- 2700, ATCC). Supernatant was harvested 18-24 h post-
714   inoculation, clarified from cellular debris by centrifugation at 2,000 x g for 5 min and concentrated
715   10 times using a 30 kDa cut off membrane and aliquoted and frozen at -80°C until use in
716   neutralization experiments. For viral neutralization, stable HRT-18G cells (ATCC) in DMEM
717   supplemented with 10% FBS, 1% PenStrep were seeded at 40,000 cells/well into clear bottom
718   white walled 96-well plates and cultured overnight at 37°C. Twelve-point 3-fold serial dilutions of
719   S2P6 were prepared in DMEM and OC43 S VSV pseudoviruses were added 1:1 (v/v) to each
720   dilution in the presence of anti-VSV-G antibody from I1- mouse hybridoma supernatant diluted 50
721   times (final volume: 50 µl). After 45 min incubation at 37℃, 40 µl of the mixture was added to the
722   cells and 2 h post-infection, another 40 µL DMEM were added to avoid evaporation. After 17-20
723   h, 50 µL/well of One-Glo-EX substrate (Promega) were added to the cells and incubated in the
724   dark for 5-10 min prior reading on a Varioskan LUX plate reader (ThermoFisher). Data was
725   processed using GraphPad Prism v9.0.
726

727   **Selection of VSV-SARS-CoV-2 mAb escape mutants**
728   *Resistant virus selection*
729   Cells were cultured in DMEM (Gibco 11995-040) supplemented with 10% FBS (VWR 97068-085
730   lot#345K19) and 100 U/ml Penicillin-Streptomycin (Gibco 15140-122). The day before infection,
731   250,000 VeroE6-TMPRSS2 cells were seeded in 12-well plates in 2 ml of DMEM (Gibco 11995-
732   040) supplemented with 10% FBS (VWR 97068-085 lot#345K19) and 100 U/ml Penicillin-
733   Streptomycin (Gibco 15140-122) and incubated overnight at 37C. The next day, S2P6 was serially
734   diluted 1:4 starting at 80 µg/ml in infection media (DMEM supplemented with 2% FBS and 20mM
735   HEPES (Gibco, 15630-080)) and incubated with replication-competent VSV-SARS-CoV-2 (23) at

736 MOI 2 for 1 hour at 37°C. A no Ab control was included to account for any tissue culture
737 adaptations and quasispecies variability that may occur during virus replication. The mAb-virus
738 complexes were adsorbed on the cells for 1 hour at 37°C, with manual rocking every 15 minutes.
739 After adsorption, cells were washed with PBS and overlaid with infection media containing an
740 equivalent amount of S2P6 as was used for the initial infection. Infection was monitored visually
741 by microscopy for GFP expression and cytopathic effect (CPE) of the cells at day 1 and day 3
742 post-infection. At day 3 post-infection, when the no mAb control well reached >50% CPE, the well
743 with the highest Ab concentration showing >20% CPE (in this case the 80 ug/ml well) was
744 selected for passaging. The cell supernatant was centrifuged to remove cell debris, diluted 1:10
745 in infection medium and added to fresh VeroE6-TMPRRS2 cells with the same S2P6
746 concentration range and treatment as for the initial passage. Selection was stopped after two
747 passages, after no virus neutralization was observed at the highest concentration tested.
748
749 *Sequencing of S gene*
750 Viral RNA was extracted from the supernatant of viral passages using the QIAamp Viral RNA Mini
751 Kit (Qiagen, 52904) according to the manufacturer's instructions, without the addition of carrier
752 RNA. Reverse transcription reactions were performed with 6 μl of purified RNA and random
753 primers using the NEB ProtoScript II First Strand cDNA Synthesis Kit (NEB, E6560S), according
754 to manufacturer's instructions. The resulting cDNA was used as a template for PCR amplification
755 of the spike gene using the KapaBiosystems polymerase (KAPA HiFi HotStart Ready PCR Kit
756 KK2601) with primers 5'- CGAGAAAAAGGCATCTGGAG -3' and 5'-
757 CATTGAACTCGTCGGTCTC -3'. Amplification conditions included an initial 3 minutes at 95°C,
758 followed by 28 cycles with 20 seconds at 98°C, 15 seconds at 59°C and 72°C for 2 minutes, with
759 a final 4 minutes at 72°C. PCR products were purified using AMPure XP beads (Beckman Coulter,
760 A63881) following manufacturer's instructions. The size of the amplicon was confirmed by
761 analyzing 2 μl of PCR products using the Agilent D5000 ScreenTape System (Agilent D5000
762 ScreenTape, 5067-5588, Agilent D5000, Reagents 5067-5589). Products were quantified by
763 analyzing 2 μl with the Quant-iT dsDNA High-Sensitivity Assay Kit (Thermo Fisher, Q331120).
764 Twenty ng of purified PCR product was used as input for library construction using the NEBNext
765 Ultra II FS DNA Library Prep Kit (NEB, E6177S) following manufacturer's instructions. DNA
766 fragmentation was performed for 13 minutes. NEBNext Multiplex Oligos for Illumina Dual Index
767 Primer Set 1 (NEB, E7600S) was used for library construction, with a total of 6 PCR cycles.
768 Libraries size was determined using the Agilent D1000 ScreenTape System (Agilent D1000
769 ScreenTape, 5067-5582, Agilent D5000 Reagents, 5067-5583) and quantified with the Quant-iT
770 dsDNA High-Sensitivity Assay Kit. Equal amounts of each library were pooled together for
771 multiplexing and 'Protocol A: Standard Normalization Method' of the Illumina library preparation
772 guide was used to prepare 8 pM final multiplexed library with 1% PhiX spike-in for sequencing.
773 The Illumina MiSeq Reagent Kit v3 (600-cycle) (Illumina, MS-102-300) was used for sequencing
774 the libraries on the Illumina MiSeq platform, with 300 cycles for Read 1, 300 cycles for Read 2, 8
775 cycles for Index 1, and 8 cycles for Index 2.
776
777 *Bioinformatic analysis*
778 The average read length after running Illumina's Bcl2fastq command was ranging from 149 to
779 188bp on average per sample. For consistency across samples, paired-end reads were initially

780   trimmed to 2X150bp and further cleaned to remove Illumina's adapter and low quality bases using
781   Trimmomatic (*62*). Read alignment was performed with Burrows- Wheeler Aligner (BWA (*63*))
782   using a custom reference sequence. Variants were called with LoFreq upon indel realignment
783   and base quality recalibration (*64*), using a frequency threshold of 1%. Two consecutive rounds
784   of alignments and variant calling were performed, where the variants called during the first round
785   at allelic frequency >50% were integrated in the reference for the second round in order to adjust
786   alignment rate and variant calling accuracy. Variants were annotated with SnpEff (*65*). The
787   reference sequence coordinates were mapped back to the SARS-CoV-2 Wuhan-Hu-1 sequence
788   (NCBI: NC_045512.2) in order to match the reference sequence nomenclature. Extensive QCs
789   were performed at read, alignment and variant level using FastQC , samtools, picard, mosdepth
790   (*66*), bcftools_(*67*), MultiQC (*68*) and in-house scripts, notably to remove variants that were
791   consistently called at a static position in reads (such as the beginning or end of reads that were
792   carrying it, rather than being randomly distributed throughout those reads.). An end-to-end
793   workflow was automated using NextFlow (*69*). All programs are available through the Bioconda
794   Initiative (*70*)(bioconda.github.io).
795

796   **Crystallization and structure determination**
797   Crystals of the S2P6 Fab/SARS-CoV peptide complex were obtained using the sitting-drop vapor
798   diffusion method at 20°C with a Fab concentration of 12 mg/ml and a 1.5x molar excess of peptide.
799   A total of 150 nl S2P6 Fab/peptide solution in 20 mM Tris-HCl pH 7.5, 50 mM NaCl were mixed
800   with 150 nl mother liquor containing 0.2 M ammonium sulfate, 0.1 M sodium acetate pH 4.6 and
801   25% (v/v) PEG Smear Broad (Molecular Dimensions). Crystals were flash frozen in liquid
802   nitrogen. Data were collected at beamline 12-2 at the Stanford Synchrotron Radiation Lightsource
803   facility in Stanford, CA. Data were processed with the XDS software package (Kabsch, 2010) for
804   a final dataset of 2.67 Å in space group $P6_522$. The S2P6 Fab/peptide complex structure was
805   solved by molecular replacement using a homology model of the S2P6 Fab built using the
806   Molecular Operating Environment (MOE) software package from the Chemical Computing Group
807   (https://www.chemcomp.com). Several subsequent rounds of model building and refinement were
808   performed using Coot (*71*), ISOLDE (*72*), Refmac5 (*73*), and MOE, to arrive at a final model for
809   the complex.
810

811   **Measurement of Fc-effector functions**
812   *MAb-dependent activation of human FcγRIIIa and FcγRIIa*
813   Determination of mAb-dependent activation of human FcγRIIIa and FcγRIIa was performed using
814   ExpiCHO cells stably expressing full-length wild-type SARS-CoV-2 spike (S) (target cells). Cells
815   were incubated with different amounts of mAbs for 10 minutes before incubation with Jurkat cells
816   stably expressing FcγRIIIa receptor (V158 variant) or FcγRIIa receptor (H131 variant) and NFAT-
817   driven luciferase gene (effector cells) at an effector to target ratio of 6:1 for FcγRIIIa and 5:1 for
818   FcγRIIa. Activation of human FcγRs was quantified by the luciferase signal produced as a result
819   of NFAT pathway activation. Luminescence was measured after 21 hours of incubation at 37˚C
820   with 5% CO_2 with a luminometer using the Bio-Glo-TM Luciferase Assay Reagent according to
821   the manufacturer's instructions (Promega, Cat. Nr.: G7018 and G9995).
822

823   *Antibody-dependent cell cytotoxicity (ADCC)*

824 ADCC assays were performed using SARS-CoV2 CHO-K1 cells (genetically engineered to stably
825 express a HaloTag-HiBit-tagged) as target cells and PBMC as effector cells at a E:T ratio of 33:1.
826 HiBit-cells were seeded at 3,000 cells/well and incubated for 16 hours at 37°C, while PBMCs
827 isolated from fresh blood (VV donor) were cultivated overnight at 37°C 5% CO_2 in the presence
828 of 5 ng/ml of IL-2. The day after, media was removed and titrated concentrations of mAbs were
829 added before the addition of PBMCs at 100,000 cells/well. As 100% specific lysis, Digitonin at
830 100 ug/ml was used. After 4 hours of incubation at 37°C, ADCC was measured with Nano-Glo
831 HiBiT Extracellular Detection System (Promega; Cat. Nr.: N2421) using a luminometer
832 (Integration Time 00:30).
833
834 *Antibody-dependent cellular phagocytosis (ADCP)*
835 ADCP was performed using CHO cells stably expressing full-length wild-type SARS-CoV-2 S
836 glycoprotein (target cells) fluorescently labelled with PKH67 Fluorescent Cell Linker Kits (Sigma
837 Aldrich; Cat. Nr.: MINI67). Target cells were incubated with titrated concentrations of mAbs for 10
838 minutes, followed by incubation with PBMCs fluorescently labelled with Cell Trace Violet
839 (Invitrogen, cat. no. C34557) after an overnight incubation in 5 ng/ml IL-2 (Recombinant Human
840 Interleukin-2; ImmunoTools GmbH; Cat. Nr.: 11340027). An effector:target ratio of 20:1 was used.
841 After an overnight incubation at 37°C, cells were stained with anti-human CD14-APC Ab (BD
842 Pharmingen, cat. no. 561708, Clone M5E2) to stain monocytes. ADCP was determined by flow
843 cytometry, gating on CD14+ cells that were double-positive for cell trace violet and PKH67.
844
845 *Complement-dependent cytotoxicity (CDC)*
846 CDC was performed on CHO cells stably expressing SARS-CoV-2 S glycoprotein (target cells)
847 incubated with serial dilutions of mAbs for 10 minutes, followed by incubation with pre-adsorbed
848 Low-Tox M Rabbit Complement (Cederlane Laboratories Limited; Cat. Nr.: CL3051) at a final
849 dilution of 1:12. CDC was measured after incubation for 3 hours at 37 °C 5% CO_2 with a
850 luminometer using the CytoTox-Glo Cytotoxicity Assay (Promega; Cat. Nr.: G9291) according to
851 the manufacturer's instructions.
852
853 **S2P6 binding and S2P6/B6 competition experiments to different synthetic coronavirus S**
854 **stem peptides**
855 All biotinylated coronavirus stem helix peptides binding experiments were performed in PBS
856 supplemented with 0.005 % Tween20 (PBST) at 30°C and 1,000 rpm shaking on an Octet Red
857 instrument (Fortebio). For S2P6 binding to different stem helix peptides, 1 µg/ml biotinylated stem
858 peptide (15- or 16-residue long stem peptide-PEG6-Lys-Biotin synthesized from Genscript) was
859 loaded on SA biosensors to a threshold of 0.5 nm. Then, the system was equilibrated in PBST for
860 300 seconds prior to immersing the sensors in 0.1 µM S2P6 mAb, respectively, for 300 seconds
861 prior to dissociation in buffer for 300 seconds. For S2P6-B6 competition, 1 µg/ml biotinylated to
862 SARS CoV-2 peptide was loaded on SA biosensors to a threshold of 0.5 nm. The system was
863 equilibrated in PBST for 180 seconds and each subsequent step was monitored for 900 seconds.
864 The first sample biosensor was immersed in 0.1 µM mAb S2P6 prior to immersing the sample
865 biosensor in a solution of 0.1 µM mAb S2P6 and B6, respectively. The second sample biosensor
866 was immersed in PBST and subsequently in 0.1 µM mAb B6. To monitor unspecific binding,
867 identical experiments were performed without loading stem peptides to the biosensors.

868

CryoEM sample preparation and data collection

869
870   1 mg/ml SARS-CoV-2 S 2P was incubated with 1.5-fold molar excess of S2M11 Fab for 30
871   minutes at 37°C (to promote the closed trimer conformation). Excess S2M11 Fab was removed
872   from the sample using a centrifugal filter (amicon ultra, 100kDa cut off). Then a 2-fold molar
873   excess of S2P6 Fab over SARS-CoV-2 S protomer was added to the solution and incubated for
874   additional 45 minutes at 37°C. 3 µl sample were applied on to a freshly glow discharged UltrAUFoil
875   Au 200 (R2/2) grid. Plunge freezing was performed using a TFS Vitrobot Mark IV (blot force: 0,
876   blot time: 6.5 s, Humidity: 100 %, temperature: 23°C). Data were acquired using a FEI Titan Krios
877   transmission electron microscope operated at 300 kV and equipped with a Gatan K3 Summit
878   direct detector and Gatan Quantum GIF energy filter, operated in zero-loss mode with a slit width
879   of 20 eV. Automated data collection was carried out using Leginon (*74*) at a nominal magnification
880   of 105,000x with a pixel size of 0.4215Å. The dose rate was adjusted to 15 counts/pixel/s, and
881   each movie was acquired in super-resolution mode fractionated in 75 frames of 40 ms. Tilted data
882   collection (45° tilt) was performed to compensate for preferential specimen orientation and 6,015
883   micrographs were collected in a single session with a defocus range comprised between 0.5 and
884   5.0 µm.

885

CryoEM data processing

886
887   Movie frame alignment, estimation of the microscope contrast-transfer function parameters,
888   particle picking and extraction were carried out using Warp (*75*). Particle images were extracted
889   with a box size of 1024 pixels^2 binned to 256 pixels^2 yielding a pixel size of 1.686 Å. Two rounds
890   of reference-free 2D classification were performed using cryoSPARC (*76*) to select well-defined
891   particle images. Subsequently, one round of 3D classification with 25 iterations was carried out
892   using Relion without imposing symmetry and using an initial ab initio model created in
893   cryoSPARC.
894   The best subclasses were combined and non-uniform refinement (NUR), defocus refinement (DR)
895   and NUR again performed in cryoSPARC. We then performed one round of global CTF
896   refinement of beam-tilt, trefoil and tetrafoil parameters followed by another refinement cycle of
897   NUR-DR-NUR. Selected particle images were then subjected to Bayesian polishing in Relion (*77*).
898   During this step the box and pixel size were changed to 426 pixels and 1.201 Å, respectively,
899   before performing another NUR-DR-NUR refinement cycle. We then performed one additional
900   round of focused classification in Relion with 25 iterations, skipping the oriental assignment and
901   using a mask covering the strongest S2P6 Fab density and a small part of the S stem to further
902   separate distinct S2P6 Fab conformations. The best classes were combined and a final round of
903   NUR performed. Reported resolutions are based on the gold-standard Fourier shell correlation
904   (FSC) of 0.143 criterion and Fourier shell correlation curves were corrected for the effects of soft
905   masking by high-resolution noise substitution (*78*).

906

CryoEM model building and analysis

907
908   UCSF Chimera (*79*) was used to fit atomic models into the cryoEM maps. The SARS-CoV-2 S
909   EM structure in complex with the variable domain of the S2M11 Fab (PDB 7K43, residue 15-
910   1140), the constant domain of the S2H14 Fab crystal structure and the S2P6-SARS-CoV-2
911   (residue 1146-1159) crystal structure were fit into the cryoEM map.

912

Fusion inhibition assay

For testing inhibition of spike-mediated cell–cell fusion Vero-E6 cells were seeded in 96 well plates at 20,000 cells/ well in 70 µl DMEM with high glucose and 2.4% FBS (Hyclone). After 16 hours, cells were transfected with SARS-CoV-2-S-D19_pcDNA3.1 as follows: for 10 wells, 0.57 µg plasmid SARS-CoV-2- S-D19_pcDNA3.1 were mixed with 1.68 µl X-tremeGENE HP in 30 µl OPTIMEM. After 15 minutes incubation, the mixture was diluted 1:10 in DMEM medium and 30 µl was added per well. A 4-fold serial dilution mAb was prepared and added to the cells, with a starting concentration of 20 µg/ml. The following day, 30 µl 5X concentrated DRAQ5 in DMEM was added per well and incubated for 2 hours at 37°C. Nine images of each well were acquired with a Cytation 5 equipment for analysis.

In vivo mAb testing using a Syrian hamster model

KU LEUVEN R&D has developed and validated a SARS-CoV-2 Syrian Golden hamster infection model (*36*).

SARS-CoV-2 virus production

The wt SARS-CoV-2 strain used in this study, BetaCov/Belgium/GHB-03021/2020 (EPI ISL 109 407976|2020-02-03), was recovered from a nasopharyngeal swab taken from an RT-qPCR confirmed asymptomatic patient who returned from Wuhan, China in the beginning of February 2020. A close relation with the prototypic Wuhan-Hu-1 2019-nCoV (GenBank accession 112 number MN908947.3) strain was confirmed by phylogenetic analysis. Infectious virus was isolated by serial passaging on HuH7 and Vero-E6 cells (*36*); passage 6 virus was used for the study described here. The titer of the virus stock was determined by end-point dilution on Vero-E6 cells by the Reed and Muench method (*80*). The variant strain B.1.351 (hCoV-19/Belgium/rega-1920/2021; EPI_ISL_896474, 2021-01-11) was isolated from nasopharyngeal swabs taken from a traveler returning to Belgium and developing respiratory symptoms. The patients' nasopharyngeal swabs were directly subjected to sequencing on a MinION platform (Oxford Nanopore) (Abdelnabi et al https://www.biorxiv.org/content/10.1101/2021.02.26.433062v1).

Live virus-related work was conducted in the high-containment A3 and BSL3+ facilities of the KU Leuven Rega Institute (3CAPS), under licenses AMV 30112018 SBB 219 2018 0892 and AMV 23102017 SBB 219 20170589 according to institutional guidelines.

SARS-CoV-2 infection model in hamsters

Wildtype Syrian hamsters (Mesocricetus auratus) were purchased from Janvier Laboratories and were housed per two in ventilated isolator cages (IsoCage N Biocontainment System, Tecniplast) with ad libitum access to food and water and cage enrichment (wood block). Housing conditions and experimental procedures were approved by the ethical committee of animal experimentation of KU Leuven (license P065-2020). Female hamsters of 6-10 weeks old were anesthetized with ketamine/xylazine/atropine and inoculated intranasally with 50 µl containing 2×10^6 or 1×10^4 TCID50 for wt or B.1.351 variant, respectively. Treatment with mAb (human or hamster S2P6 (2-20 mg/kg) was initiated either 24) or 48 hours before infection by intraperitoneal injection. Hamsters were monitored for appearance, behavior and body weight. At day 4 post-infection, hamsters were euthanized by intraperitoneal injection of 500 µl Dolethal (200 mg/ml sodium

956   pentobarbital, Vétoquinol SA). Lungs were collected, and viral RNA and infectious virus were
957   quantified by RT-qPCR and end-point virus titration, respectively. Blood samples were collected
958   before infection for pharmacokinetics analysis.
959
960   *SARS-CoV-2 RT-qPCR*
961   Hamster tissues were collected after sacrifice and were homogenized using bead disruption
962   (Precellys) in 350 µl RLT buffer (RNeasy Mini kit, Qiagen) and centrifuged (10,000 rpm, 5 minutes)
963   to pellet the cell debris. RNA was extracted according to the manufacturer's instructions. To
964   extract RNA from serum, a NucleoSpin kit (Macherey-Nagel) was used. 4 µl out of 50 µl eluate
965   were used as a template in RT-qPCR reactions. RT-qPCR was performed on a LightCycler96
966   platform (Roche) using the iTaq Universal Probes One-Step RTqPCR kit (BioRad) with N2
967   primers and probes targeting the nucleocapsid (*36*). Standards of SARS-CoV-2 cDNA (IDT) were
968   used to express viral genome copies per mg tissue or per ml serum.
969
970   *End-point virus titrations*
971   Lung tissues were homogenized using bead disruption (Precellys) in 350 µl minimal essential
972   medium and centrifuged (10,000 rpm, 5 minutes, 4°C) to pellet the cell debris. To quantify
973   infectious SARS-CoV-2 particles, endpoint titrations were performed on confluent Vero-E6 cells
974   in 96-well plates. Viral titers were calculated by the Reed and Muench method (*80*) using the
975   Lindenbach calculator and were expressed as 50% tissue culture infectious dose (TCID50) per
976   mg tissue.
977
978

979 **Supplementary Information**

980

981 **Table S1: CryoEM data collection and refinement statistics.**

982

	S2P6/SARS-CoV-2 S (C3 map, post polishing)	S2P6/SARS-CoV-2 S (C1 map, before polishing)
Data collection		
Magnification		105,000
Voltage (kV)		300
Total exposure ($e^-/Å^2$)		60
Defocus range (μm)		-0.1 to -5
Pixel size (Å)		1.201
Initial particle stack		1,092,473
Final particle stack		81,519
Map resolution (0.143 FSC threshold) (Å)		4.2
Map B-factor		102.2
Symmetry		C1

983

984 **Table S2: X-ray crystallography data collection and refinement statistics.**

985

	S2P6/SARS-CoV-2
Data collection	
Space group	$P6_522$
Cell dimensions	
a, b, c (Å)	92.64, 92.64, 223.41
α, β, γ (°)	90.00, 90.00, 120.00
Resolution (Å)	46.32-2.67 (2.80-2.67) *
R_{merge}	0.203 (3.714)
$I / \sigma I$	8.9 (0.6)
Completeness (%)	99.0 (99.7)
Redundancy	8.0 (8.4)
Refinement	
Resolution (Å)	2.67
No. reflections	16,392
R_{work} / R_{free}	0.243/0.280
No. atoms	
Protein	3,054
Ligand/ion	26
Water	52
B-factors	
Protein	88.37
Ligand/ion	87.00
Water	63.77
R.m.s. deviations	
Bond lengths (Å)	0.002
Bond angles (°)	0.479

986

987

A

| mAb | HEAVY CHAIN | | | | | LIGHT CHAIN | | | | |
	IGHV	IGHD	IGHV	CDR3-length (amino acid)	V identity (%)	IGLV	IGLJ	CDR3-length (amino acid)	V identity (%)	Time point from disease onset
S2P6	V1-46*01	D5-12*01	J4*03	11	95.14	KV3-20*01	K3*01	11	97.52	46
S2S43	V1-46*01	D5-12*01	J6*02	10	96.53	LV1-51*02	J1*01	11	94.74	39
P34D10	V3-30*03	D3-9*01	J6*02	14	90.28	LV2-23*02	J3*02	11	97.22	43
P34G12	V3-30*03	D3-9*01	J6*02	14	87.85	LV2-23*02	J3*02	11	94.10	43
P34E3	V3-30*03	D3-9*01	J6*02	14	86.46	LV2-23*02	J3*02	11	95.14	43
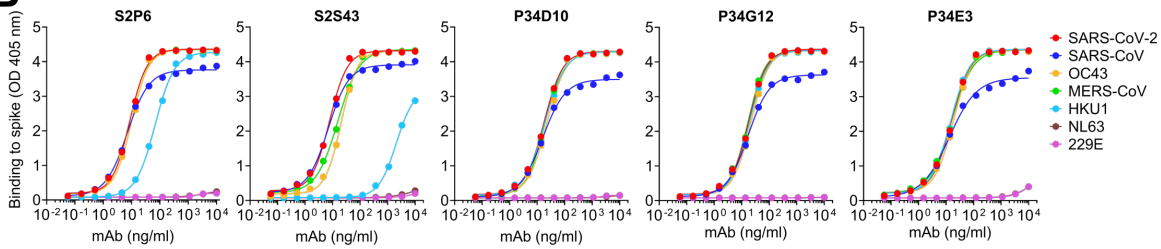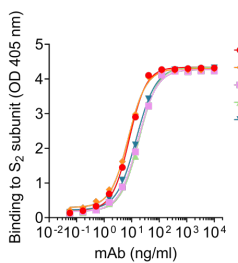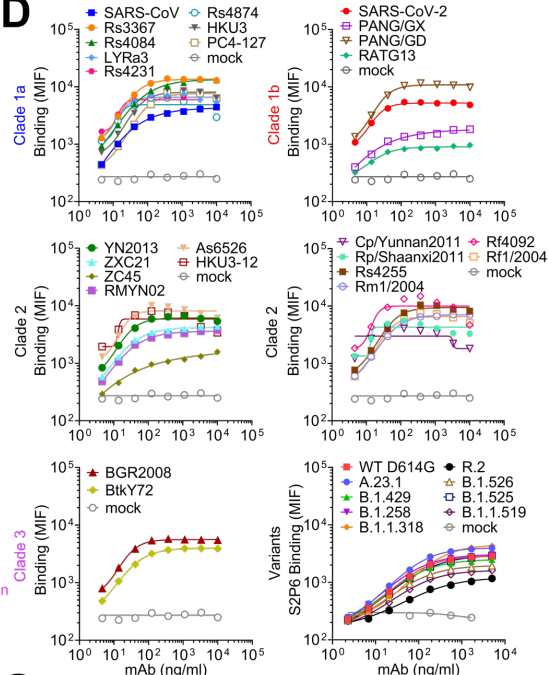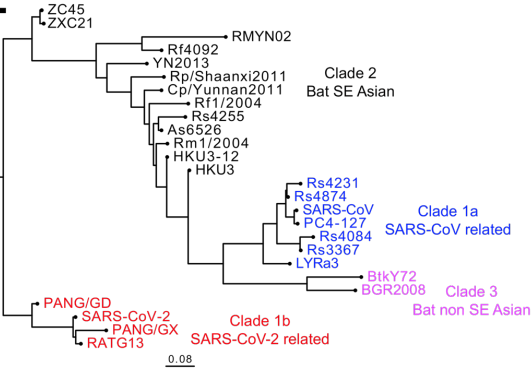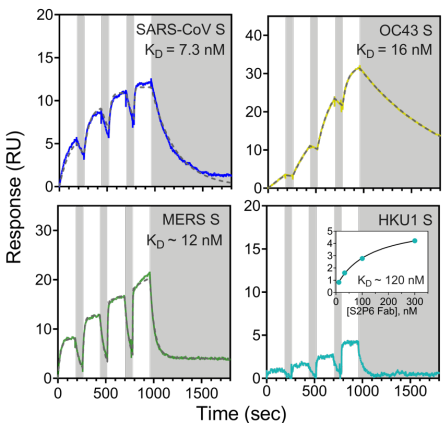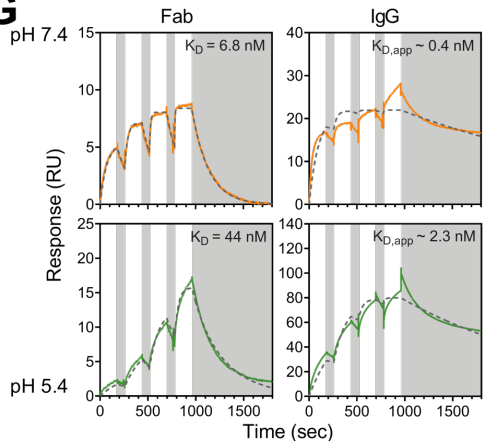
989 **Fig. S1. Properties of the 5 cross-reactive mAbs isolated.** (**A**) V(D)J usage, nucleotide
990 sequence identity to germline genes, number of somatic mutations, and time interval between
991 sample collection and mAb isolation. (**B**) Binding of identified mAbs to prefusion β-coronavirus S
992 ectodomain trimers by ELISA (**C**) Binding to SARS-CoV-2 post-fusion S_2 subunit. (**D**) Mean
993 fluorescence intensity as measured in flow cytometry for S2P6 binding to a panel of 26 S
994 glycoproteins representative of all *sarbecovirus* clades and 8 SARS-CoV-2 variants. (**E**)
995 Phylogenetic tree of sarbecoviruses S used in this work inferred via maximum likelihood analysis
996 of spike amino acid sequences. (**F**) SPR analysis of S2P6 Fab binding to immobilized prefusion
997 β-coronavirus S trimers. (**G**) SPR analysis of S2P6 Fab and IgG binding to immobilized prefusion
998 SARS-CoV-2 S ectodomain trimer at pH 7.4 and pH 5.4. Fits to a 1:1 binding model are an
999 approximation for IgG binding due to bivalency.
1000
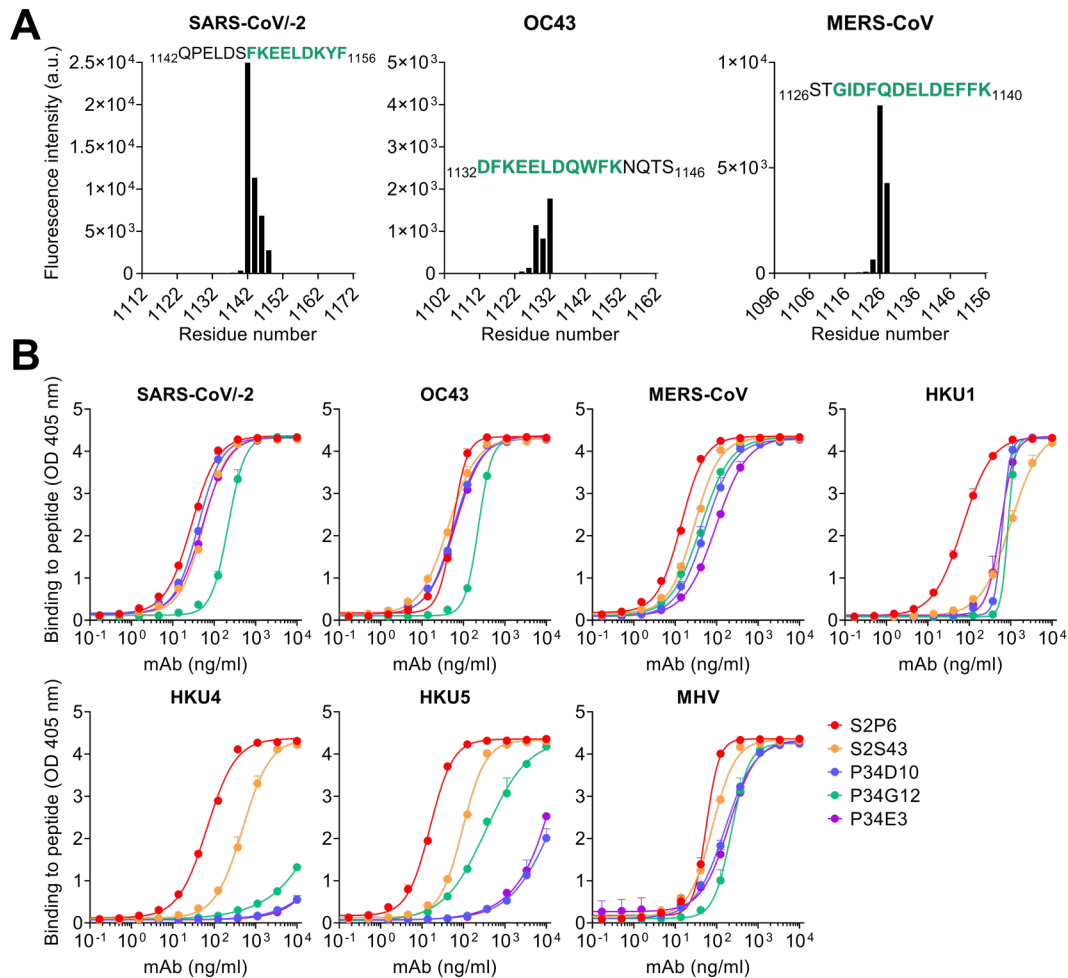
Fig. S2. Identification of the S2P6 epitope. (**A**) Binding of S2P6 to linear peptides (15-mer peptides overlapping by 13 residues) spanning the SARS-CoV/SARS-CoV-2 S, OC43 S and MERS-CoV S sequences. (**B**) Binding of identified mAbs to β-coronavirus S stem helix peptides by ELISA.
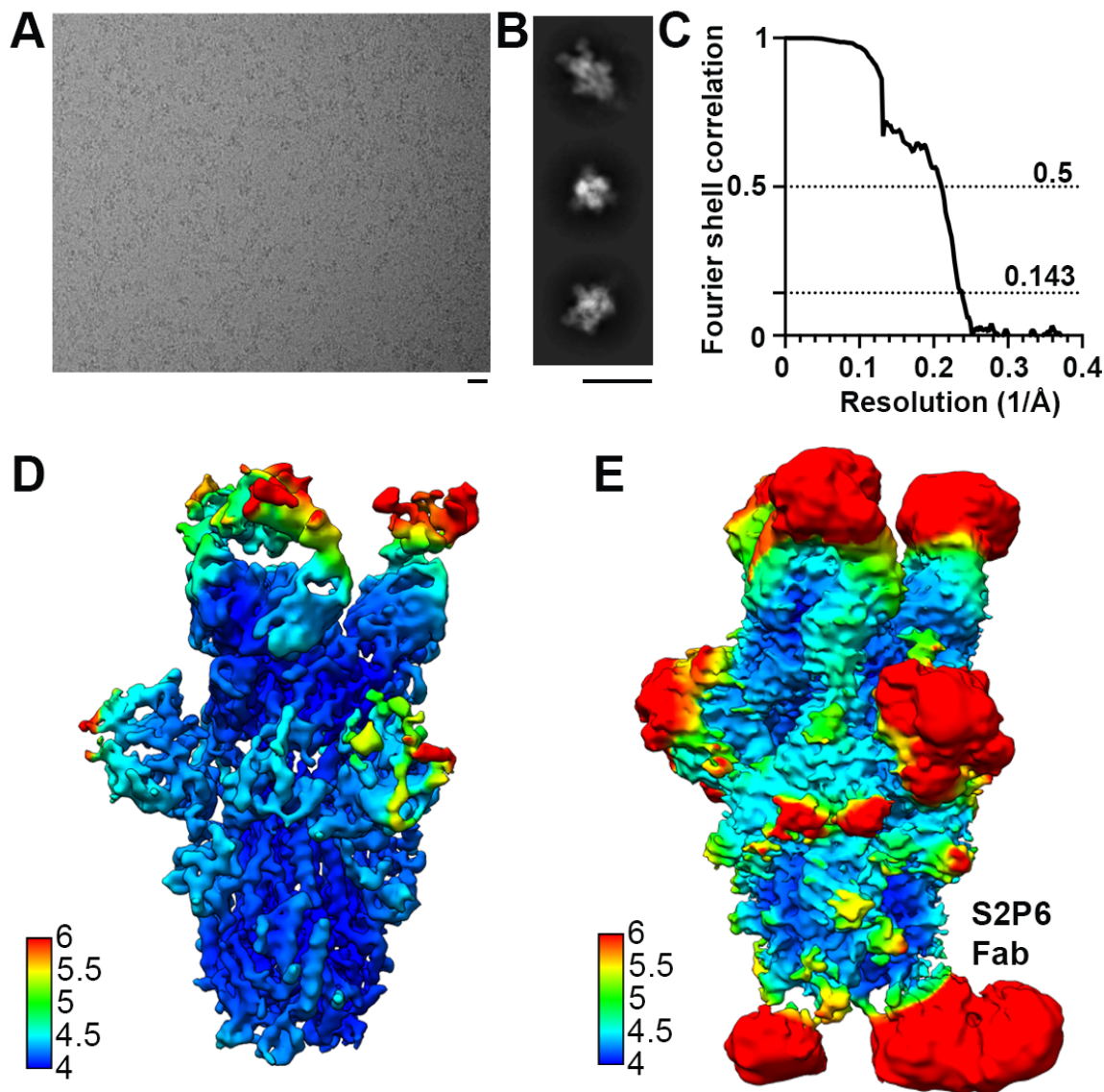
1008

Fig. S3. **CryoEM data processing and validation of S2P6- and S2M11-bound SARS-CoV-2 S dataset.** (**A-B**) Representative electron micrographs (A) and class averages (B) of SARS-CoV-2 S in complex with the S2P6 and S2M11 Fabs. Scale bars: 200 Å. (**C**) Gold-standard Fourier shell correlation curve. The 0.143 and 0.5 cut-offs are indicated by horizontal dashed gray lines. (**D-E**) CryoEM map colored by local resolution computed using cryoSPARC shown at two distinct contour levels.

1009

A Omit 2Fo-Fc density at 1σ

B S2P6/SARS-CoV/-2

D Post-fusion S
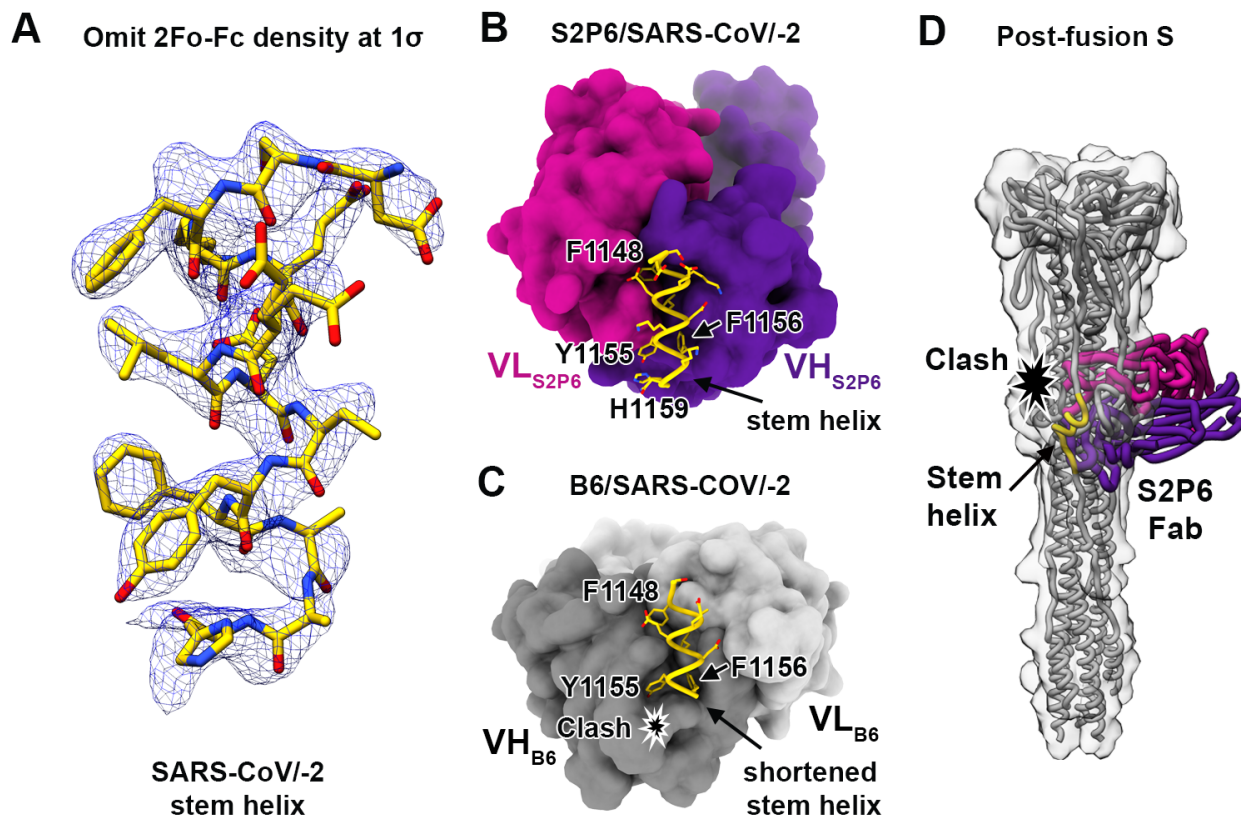
C B6/SARS-COV/-2

1010

Fig. S4. Comparison of the S2P6 and B6 mAb binding modes. (**A**) Crystal structure of the SARS-CoV-2 stem helix peptide rendered as sticks with the corresponding 2Fo-Fc omit map contoured at 1.5σ. The S2P6 Fab fragment is not shown for clarity. (**B**) Crystal structure of the S2P6 Fab (surface rendering) in complex with the SARS-CoV-2 S stem helix peptide (yellow ribbon with side chains rendered as sticks). (**C**) Crystal structure of the B6 Fab (surface rendering) in complex with the SARS-CoV-2 S stem helix peptide (yellow ribbon with side chains rendered as sticks). The star indicates the putative clash between B6 CDRH2 and the stem helix C-terminus, likely explaining the latter region is disordered in the B6-bound structure whereas it is resolved in the S2P6-bound structure. (**D**) Superimposition of the S2P6-bound (purple/magenta) SARS-CoV-2 stem helix (yellow) crystal structure onto the SARS-CoV S post-fusion structure (PDB 6M3W) shows that S2P6 binding would be incompatible due to steric hindrance suggesting S2P6 prevents S fusogenic conformational changes. A low-pass filtered surface generated from the SARS-CoV S post-fusion structure is shown as a transparent gray surface to help visualizing clashes.
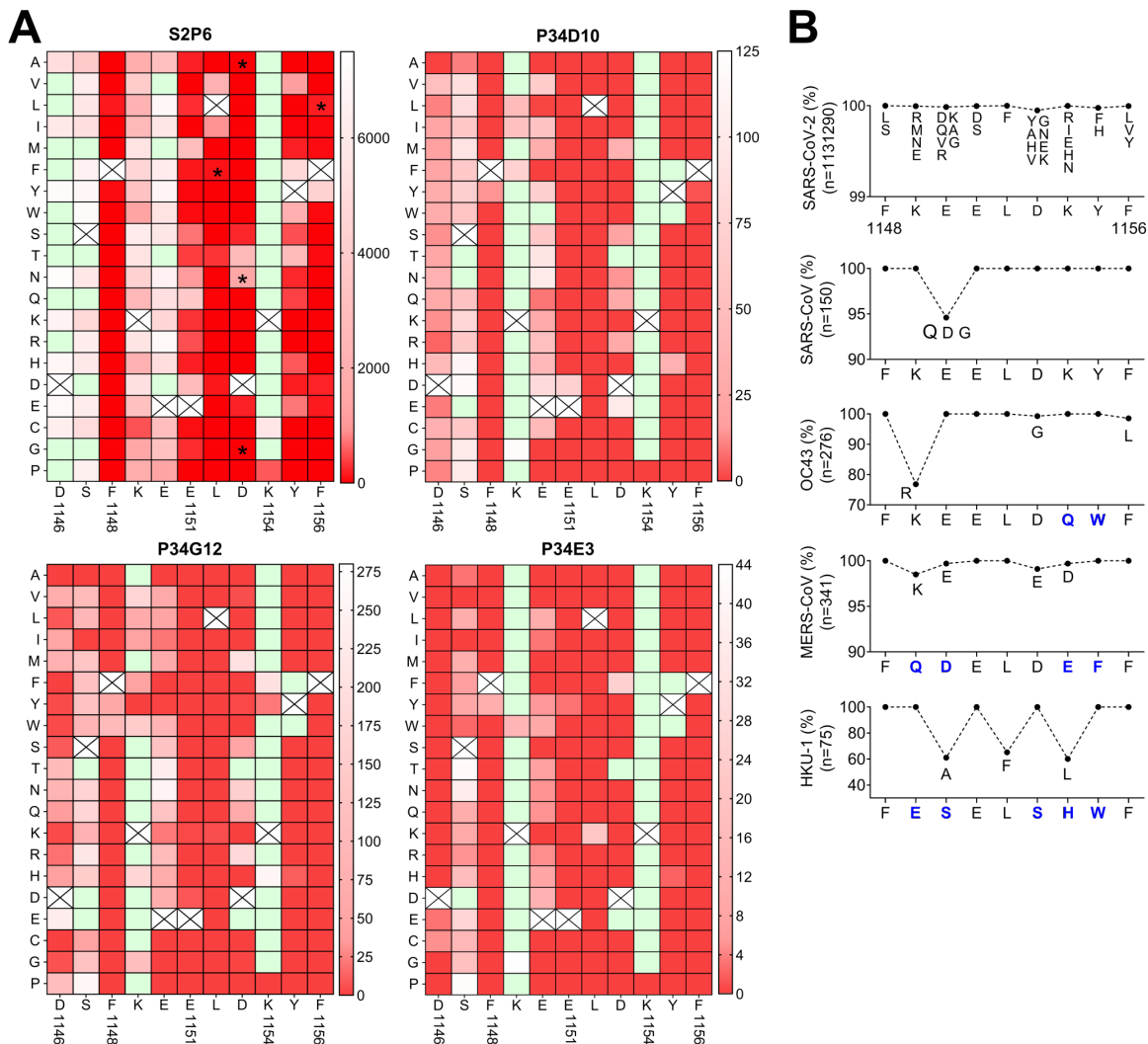
Fig. S5. **Impact of individual SARS-CoV-2 stem helix residue substitution on mAb binding.**
(**A**) Heat map showing binding (fluorescence intensity) of S2P6, P34D10, P34G12 and P34E3 to stem helix peptides harboring each possible amino acid substitution. White to red gradient indicate the degree of loss of binding as compared to the native residue (white) shown as a crossed square. Green squares indicate substitutions enhancing binding as compared to the native residue. Asterisks highlight viral escape substitutions identified in vitro for S2P6. (**B**) Epitope conservation among β-coronavirus sequences with human and animal hosts retrieved from GISAID. The consensus sequence for SARS-CoV-2 is reported on x axis and predominant substitutions are indicated by a blue letter.

A

Convalescent donor demographics		
Participants		72
Sex	Female	35
	Male	37
	N/A	3
Age	Average	50
	Range	18-77
Days after symptom onset		
	Range	13-105
Hospitalized		15
	Clinica Luganese Moncucco	3
	Luigi Sacco Hospital	12
Symptomatic		54
	Clinica Luganese Moncucco	7
	Luigi Sacco Hospital	1
	Swiss volunteers	20
	US - San Francisco	26
Asymptomatic		6
	Luigi Sacco Hospital	2
	Swiss volunteers	2
	US - San Francisco	2

Vaccinated donor demographics		
Participants		46
Sex	Female	18
	Male	28
Age	Average	70
	Range	28-91
SARS-CoV-2	Naïve	37
	Immune	7
Vaccine	Dose 1	3
	Dose 2	43

B

Convalescent donor demographics		
Participants		21
Sex	Female	12
	Male	9
	N/A	0
Age	Average	41
	Range	21-54
Days after PCR positive test		
	Range	207-254
Symptomatic		10
	Ente Ospedaliero Cantonale	
Asymptomatic		11
	Ente Ospedaliero Cantonale	

Fig. S6. Patient demographics. (**A**) Summary of convalescent patient demographics from which plasma (left table) or memory repertoire (right table) have been analyzed. (**B**) Summary of vaccinees patient demographics.
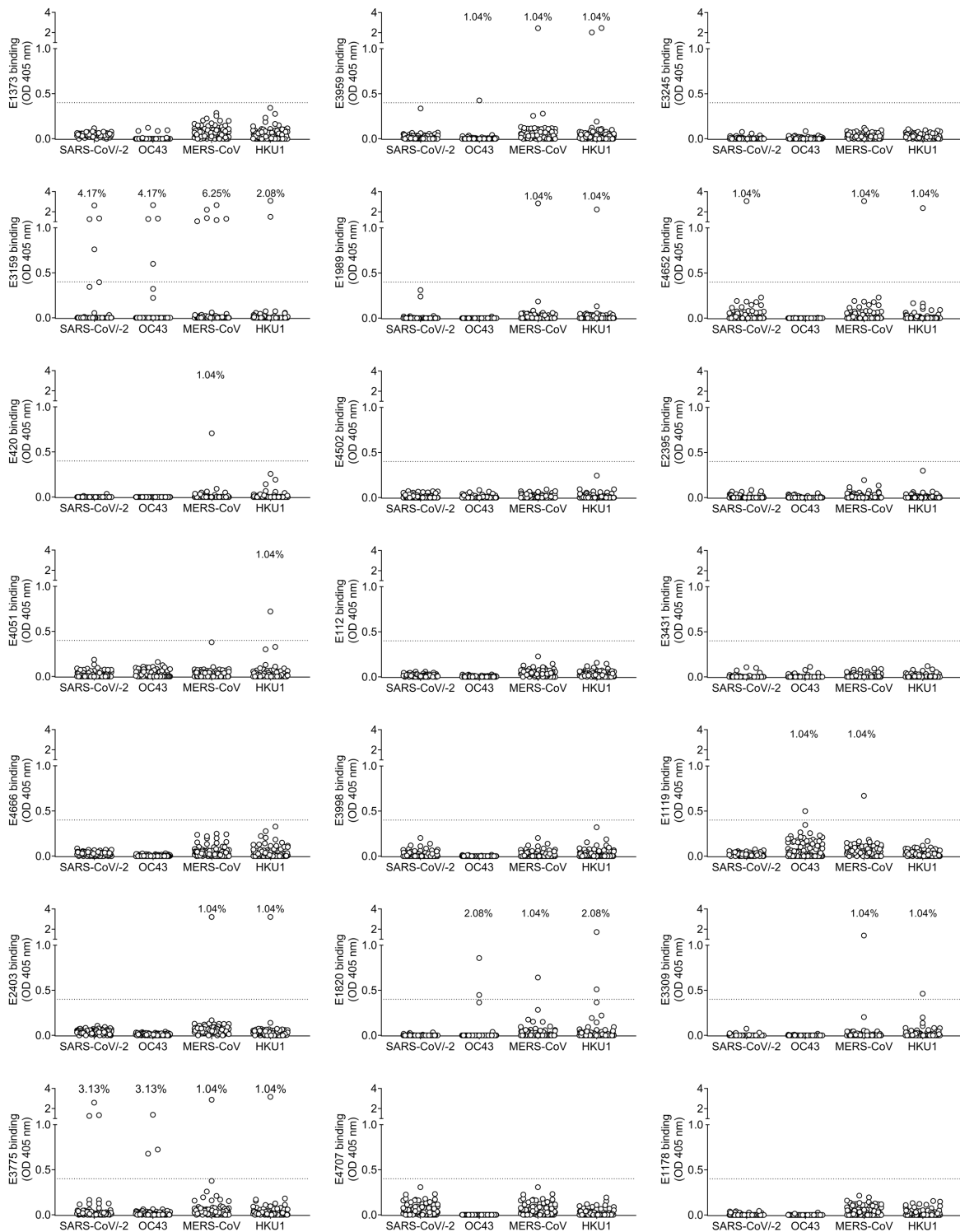
Fig. S7. **Binding of IgG memory B-cells from COVID-19 convalescent individuals to β-coronavirus stem helix peptides.** Cut-off (OD=0.4) is indicated by a dotted line and frequencies of cultures scoring positive are reported for each antigen.
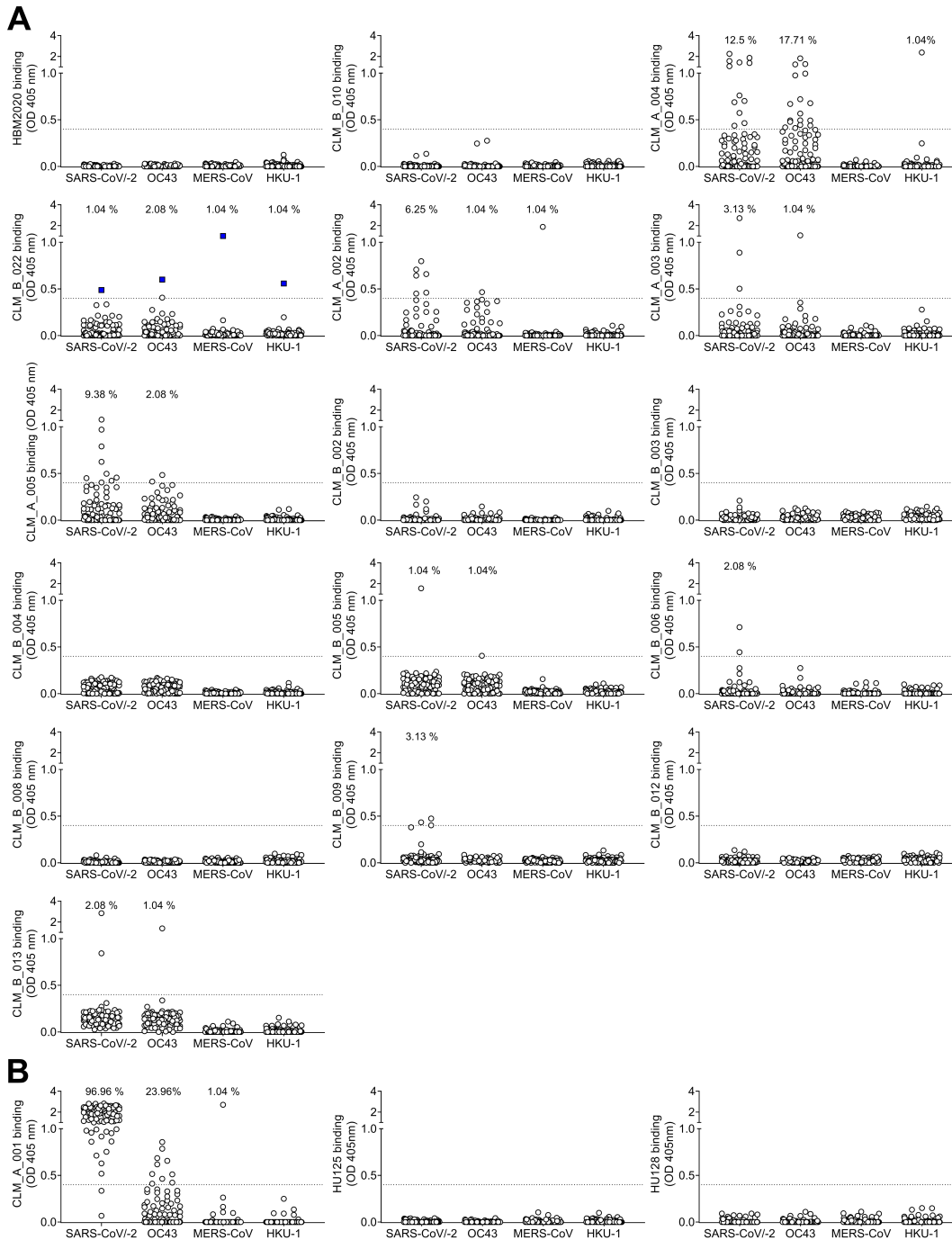
Fig. S8. **Binding of IgG memory B-cells from COVID-19 vaccinees to β-coronavirus stem helix peptides.** (**A**) Cut-off (OD=0.4) is indicated by a dotted line and frequencies of cultures scoring positive are reported for each antigen. (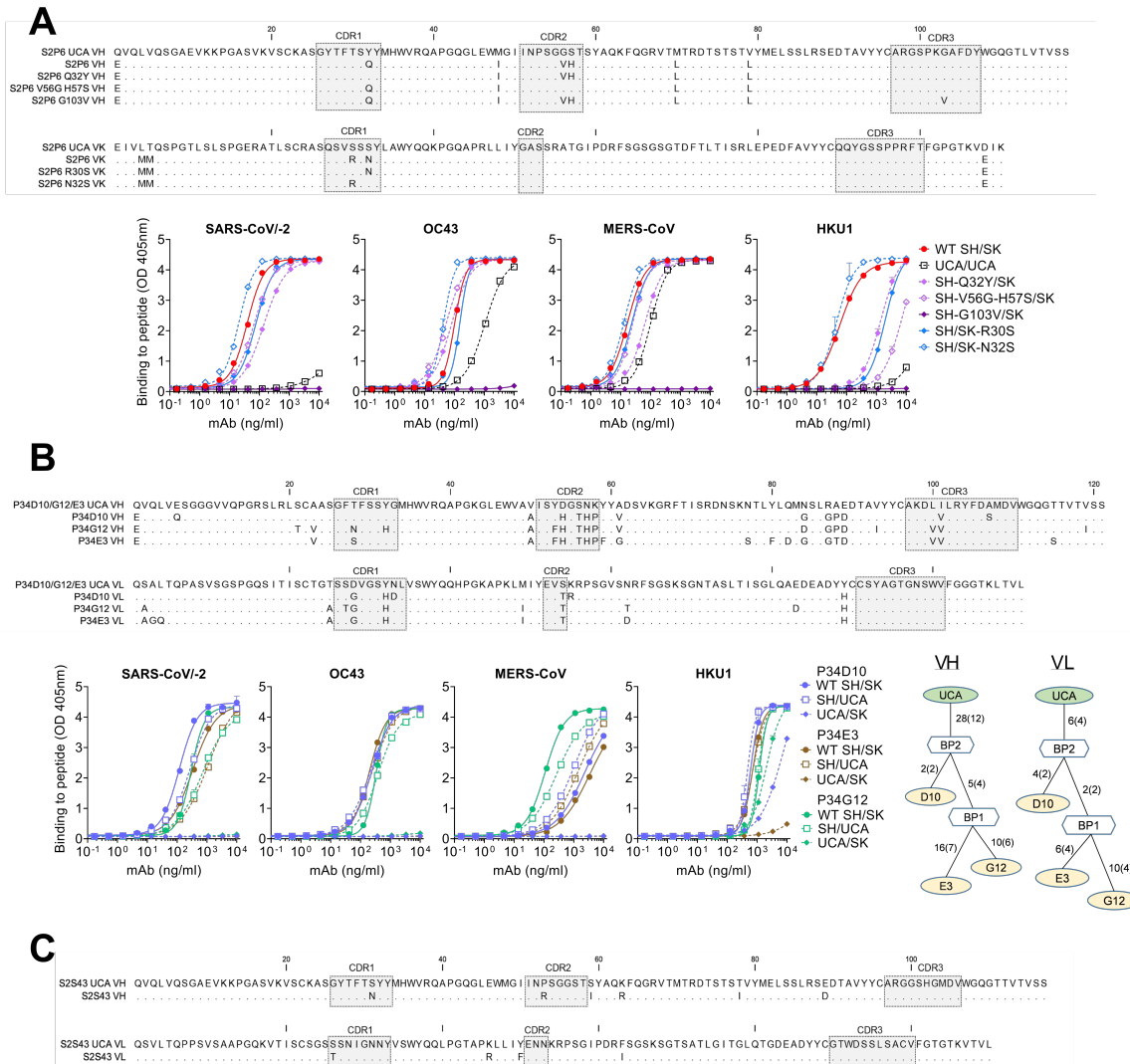**B**) Binding to stem helix peptide of a previously infected individual after first vaccine dose showing high response to SARS-CoV-2 (left) and of two pre-pandemic individuals (middle and right).

1057

1058
1059

Fig. S9. Analysis of mAbs sequence. (**A**) Alignment of the amino acid sequences of S2P6 UCA and wild-type VH and VL (top). The CDRs regions are highlighted in gray. Binding of S2P6 mutated SH or SK with fully germline reverted residues in CDR (bottom). (**B**) Alignment of the amino acid sequences of P34D10, P34G12 and P34E3 UCA and wild-type VH and VL (top). Binding of mAbs mature heavy chain paired with germline reverted light chain (SH/UCA) and germline reverted heavy chain paired with mature light chain (UCA/SK) (bottom). Genealogic trees of VH and VL genes of P34D10, P34G12 and P34E3 shown using AncesTree (*81*). The number of nucleotide and amino acid (in parentheses) mutations from the unmutated common ancestor (UCA) or branch points (BPs) to their descendants are shown. (**C**) Alignment of the amino acid sequences of S2S43 UCA and wild-type VH and VL

1070

References:

1. P. Zhou, X. L. Yang, X. G. Wang, B. Hu, L. Zhang, W. Zhang, H. R. Si, Y. Zhu, B. Li, C. L. Huang, H. D. Chen, J. Chen, Y. Luo, H. Guo, R. D. Jiang, M. Q. Liu, Y. Chen, X. R. Shen, X. Wang, X. S. Zheng, K. Zhao, Q. J. Chen, F. Deng, L. L. Liu, B. Yan, F. X. Zhan, Y. Y. Wang, G. F. Xiao, Z. L. Shi, A pneumonia outbreak associated with a new coronavirus of probable bat origin. *Nature* (2020), doi:10.1038/s41586-020-2012-7.

2. M. A. Tortorici, D. Veesler, Structural insights into coronavirus entry. *Adv. Virus Res.* **105**, 93–116 (2019).

3. A. C. Walls, Y. J. Park, M. A. Tortorici, A. Wall, A. T. McGuire, D. Veesler, Structure, Function, and Antigenicity of the SARS-CoV-2 Spike Glycoprotein. *Cell*. **181**, 281-292.e6 (2020).

4. D. Wrapp, N. Wang, K. S. Corbett, J. A. Goldsmith, C. L. Hsieh, O. Abiona, B. S. Graham, J. S. McLellan, Cryo-EM structure of the 2019-nCoV spike in the prefusion conformation. *Science*. **367**, 1260–1263 (2020).

5. E. C. Thomson, L. E. Rosen, J. G. Shepherd, R. Spreafico, A. da Silva Filipe, J. A. Wojcechowskyj, C. Davis, L. Piccoli, D. J. Pascall, J. Dillen, S. Lytras, N. Czudnochowski, R. Shah, M. Meury, N. Jesudason, A. De Marco, K. Li, J. Bassi, A. O'Toole, D. Pinto, R. M. Colquhoun, K. Culap, B. Jackson, F. Zatta, A. Rambaut, S. Jaconi, V. B. Sreenu, J. Nix, I. Zhang, R. F. Jarrett, W. G. Glass, M. Beltramello, K. Nomikou, M. Pizzuto, L. Tong, E. Cameroni, T. I. Croll, N. Johnson, J. Di Iulio, A. Wickenhagen, A. Ceschi, A. M. Harbison, D. Mair, P. Ferrari, K. Smollett, F. Sallusto, S. Carmichael, C. Garzoni, J. Nichols, M. Galli, J. Hughes, A. Riva, A. Ho, M. Schiuma, M. G. Semple, P. J. M. Openshaw, E. Fadda, J. K. Baillie, J. D. Chodera, S. J. Rihn, S. J. Lycett, H. W. Virgin, A. Telenti, D. Corti, D. L. Robertson, G. Snell, Circulating SARS-CoV-2 spike N439K variants maintain fitness while evading antibody-mediated immunity. *Cell* (2021), doi:10.1016/j.cell.2021.01.037.

6. M. McCallum, A. De Marco, F. A. Lempp, M. A. Tortorici, D. Pinto, A. C. Walls, M. Beltramello, A. Chen, Z. Liu, F. Zatta, S. Zepeda, J. di Iulio, J. E. Bowen, M. Montiel-Ruiz, J. Zhou, L. E. Rosen, S. Bianchi, B. Guarino, C. S. Fregni, R. Abdelnabi, S.-Y. Caroline Foo, P. W. Rothlauf, L.-M. Bloyet, F. Benigni, E. Cameroni, J. Neyts, A. Riva, G. Snell, A. Telenti, S. P. J. Whelan, H. W. Virgin, D. Corti, M. S. Pizzuto, D. Veesler, N-terminal domain antigenic mapping reveals a site of vulnerability for SARS-CoV-2. *Cell* (2021), doi:10.1016/j.cell.2021.03.028.

7. K. R. McCarthy, L. J. Rennick, S. Nambulli, L. R. Robinson-McCarthy, W. G. Bain, G. Haidar, W. P. Duprex, Recurrent deletions in the SARS-CoV-2 spike glycoprotein drive antibody escape. *Science* (2021), doi:10.1126/science.abf6950.

8. B. Choi, M. C. Choudhary, J. Regan, J. A. Sparks, R. F. Padera, X. Qiu, I. H. Solomon, H. H. Kuo, J. Boucau, K. Bowman, U. D. Adhikari, M. L. Winkler, A. A. Mueller, T. Y. Hsu, M. Desjardins, L. R. Baden, B. T. Chan, B. D. Walker, M. Lichterfeld, M. Brigl, D. S. Kwon, S. Kanjilal, E. T. Richardson, A. H. Jonsson, G. Alter, A. K. Barczak, W. P. Hanage, X. G. Yu, G. D. Gaiha, M. S. Seaman, M. Cernadas, J. Z. Li, Persistence and Evolution of SARS-CoV-2 in an Immunocompromised Host. *N. Engl. J. Med.* (2020), doi:10.1056/NEJMc2031364.

9. Z. Liu, L. A. VanBlargan, L.-M. Bloyet, P. W. Rothlauf, R. E. Chen, S. Stumpf, H. Zhao, J. M. Errico, E. S. Theel, M. J. Liebeskind, B. Alford, W. J. Buchser, A. H. Ellebedy, D. H. Fremont, M. S. Diamond, S. P. J. Whelan, Identification of SARS-CoV-2 spike mutations that attenuate monoclonal and serum antibody neutralization. *Cell Host Microbe* (2021), doi:10.1016/j.chom.2021.01.014.

10. Y. Weisblum, F. Schmidt, F. Zhang, J. DaSilva, D. Poston, J. C. C. Lorenzi, F. Muecksch, M. Rutkowska, H.-H. Hoffmann, E. Michailidis, C. Gaebler, M. Agudelo, A. Cho, Z. Wang, A. Gazumyan, M. Cipolla, L. Luchsinger, C. D. Hillyer, M. Caskey, D. F. Robbiani, C. M. Rice, M. C. Nussenzweig, T. Hatziioannou, P. D. Bieniasz, Escape from neutralizing antibodies by SARS-CoV-2 spike protein variants. *Elife*. **9**, e61312 (2020).

11. A. C. Walls, X. Xiong, Y. J. Park, M. A. Tortorici, J. Snijder, J. Quispe, E. Cameroni, R. Gopal, M. Dai, A. Lanzavecchia, M. Zambon, F. A. Rey, D. Corti, D. Veesler, Unexpected Receptor Functional Mimicry Elucidates Activation of Coronavirus Fusion. *Cell*. **176**, 1026-1039.e15 (2019).

12. M. M. Sauer, M. A. Tortorici, Y.-J. Park, A. C. Walls, L. Homad, O. Acton, J. Bowen, C. Wang, X. Xiong, W. de van der Schueren, J. Quispe, B. G. Hoffstrom, B.-J. Bosch, A. T. McGuire, D. Veesler, Structural basis for broad coronavirus neutralization. *bioRxiv* (2020), doi:10.1101/2020.12.29.424482.

13. C. Wang, R. van Haperen, J. Gutiérrez-Álvarez, W. Li, N. M. A. Okba, I. Albulescu, I. Widjaja, B. van Dieren, R. Fernandez-Delgado, I. Sola, D. L. Hurdiss, O. Daramola, F. Grosveld, F. J. M. van Kuppeveld, B. L. Haagmans, L. Enjuanes, D. Drabek, B.-J. Bosch, A conserved immunogenic and vulnerable site on the coronavirus spike protein delineated by cross-reactive monoclonal antibodies. *Nat. Commun.* **12**, 1715 (2021).

14. G. Song, W.-T. He, S. Callaghan, F. Anzanello, D. Huang, J. Ricketts, J. L. Torres, N. Beutler, L. Peng, S. Vargas, J. Cassell, M. Parren, L. Yang, C. Ignacio, D. M. Smith, J. E. Voss, D. Nemazee, A. B. Ward, T. Rogers, D. R. Burton, R. Andrabi, *bioRxiv*, in press.

15. N. L. Kallewaard, D. Corti, P. J. Collins, U. Neu, J. M. McAuliffe, E. Benjamin, L. Wachter-Rosati, F. J. Palmer-Hill, A. Q. Yuan, P. A. Walker, M. K. Vorlaender, S. Bianchi, B. Guarino, A. De Marco, F. Vanzetta, G. Agatic, M. Foglierini, D. Pinna, B. Fernandez-Rodriguez, A. Fruehwirth, C. Silacci, R. W. Ogrodowicz, S. R. Martin, F. Sallusto, J. A. Suzich, A. Lanzavecchia, Q. Zhu, S. J. Gamblin, J. J. Skehel, Structure and Function Analysis of an Antibody Recognizing All Influenza A Subtypes. *Cell*. **166**, 596–608 (2016).

16. B. F. Haynes, D. R. Burton, J. R. Mascola, Multiple roles for HIV broadly neutralizing antibodies. *Sci. Transl. Med.* **11**, eaaz2686 (2019).

17. M. Hoffmann, K. Mösbauer, H. Hofmann-Winkler, A. Kaul, H. Kleine-Weber, N. Krüger, N. C. Gassen, M. A. Müller, C. Drosten, S. Pöhlmann, Chloroquine does not inhibit infection of human lung cells with SARS-CoV-2. *Nature*. **585**, 588–590 (2020).

18. M. Hoffmann, H. Kleine-Weber, S. Schroeder, N. Krüger, T. Herrler, S. Erichsen, T. S. Schiergens, G. Herrler, N. H. Wu, A. Nitsche, M. A. Müller, C. Drosten, S. Pöhlmann, SARS-CoV-2 Cell Entry Depends on ACE2 and TMPRSS2 and Is Blocked by a Clinically Proven Protease Inhibitor. *Cell*. **181**, 271-280.e8 (2020).

1155 19. M. Hoffmann, H. Kleine-Weber, S. Pöhlmann, A Multibasic Cleavage Site in the Spike
1156   Protein of SARS-CoV-2 Is Essential for Infection of Human Lung Cells. *Mol. Cell*. **78**, 779-
1157   784.e5 (2020).

1158 20. Y. Kaname, H. Tani, C. Kataoka, M. Shiokawa, S. Taguwa, T. Abe, K. Moriishi, T.
1159   Kinoshita, Y. Matsuura, Acquisition of complement resistance through incorporation of
1160   CD55/decay-accelerating factor into viral particles bearing baculovirus GP64. *J. Virol.* **84**,
1161   3210–3219 (2010).

1162 21. D. Pinto, Y. J. Park, M. Beltramello, A. C. Walls, M. A. Tortorici, S. Bianchi, S. Jaconi, K.
1163   Culap, F. Zatta, A. De Marco, A. Peter, B. Guarino, R. Spreafico, E. Cameroni, J. B. Case,
1164   R. E. Chen, C. Havenar-Daughton, G. Snell, A. Telenti, H. W. Virgin, A. Lanzavecchia, M.
1165   S. Diamond, K. Fink, D. Veesler, D. Corti, Cross-neutralization of SARS-CoV-2 by a human
1166   monoclonal SARS-CoV antibody. *Nature*. **583**, 290–295 (2020).

1167 22. M. A. Tortorici, M. Beltramello, F. A. Lempp, D. Pinto, H. V. Dang, L. E. Rosen, M.
1168   McCallum, J. Bowen, A. Minola, S. Jaconi, F. Zatta, A. De Marco, B. Guarino, S. Bianchi,
1169   E. J. Lauron, H. Tucker, J. Zhou, A. Peter, C. Havenar-Daughton, J. A. Wojcechowskyj, J.
1170   B. Case, R. E. Chen, H. Kaiser, M. Montiel-Ruiz, M. Meury, N. Czudnochowski, R.
1171   Spreafico, J. Dillen, C. Ng, N. Sprugasci, K. Culap, F. Benigni, R. Abdelnabi, S. C. Foo, M.
1172   A. Schmid, E. Cameroni, A. Riva, A. Gabrieli, M. Galli, M. S. Pizzuto, J. Neyts, M. S.
1173   Diamond, H. W. Virgin, G. Snell, D. Corti, K. Fink, D. Veesler, Ultrapotent human
1174   antibodies protect against SARS-CoV-2 challenge via multiple mechanisms. *Science*. **370**,
1175   950–957 (2020).

1176 23. J. B. Case, P. W. Rothlauf, R. E. Chen, Z. Liu, H. Zhao, A. S. Kim, L. M. Bloyet, Q. Zeng,
1177   S. Tahan, L. Droit, M. X. G. Ilagan, M. A. Tartell, G. Amarasinghe, J. P. Henderson, S.
1178   Miersch, M. Ustav, S. Sidhu, H. W. Virgin, D. Wang, S. Ding, D. Corti, E. S. Theel, D. H.
1179   Fremont, M. S. Diamond, S. P. J. Whelan, Neutralizing Antibody and Soluble ACE2
1180   Inhibition of a Replication-Competent VSV-SARS-CoV-2 and a Clinical Isolate of SARS-
1181   CoV-2. *Cell Host Microbe*. **28**, 475-485.e5 (2020).

1182 24. M. Gui, W. Song, H. Zhou, J. Xu, S. Chen, Y. Xiang, X. Wang, Cryo-electron microscopy
1183   structures of the SARS-CoV spike glycoprotein reveal a prerequisite conformational state
1184   for receptor binding. *Cell Res.* **27**, 119–129 (2017).

1185 25. R. N. Kirchdoerfer, N. Wang, J. Pallesen, D. Wrapp, H. L. Turner, C. A. Cottrell, K. S.
1186   Corbett, B. S. Graham, J. S. McLellan, A. B. Ward, Stabilized coronavirus spikes are
1187   resistant to conformational changes induced by receptor recognition or proteolysis. *Sci.*
1188   *Rep.* **8**, 15701 (2018).

1189 26. Y. Yuan, D. Cao, Y. Zhang, J. Ma, J. Qi, Q. Wang, G. Lu, Y. Wu, J. Yan, Y. Shi, X. Zhang,
1190   G. F. Gao, Cryo-EM structures of MERS-CoV and SARS-CoV spike glycoproteins reveal
1191   the dynamic receptor binding domains. *Nat. Commun.* **8**, 15092 (2017).

1192 27. A. C. Walls, M. A. Tortorici, J. Snijder, X. Xiong, B. J. Bosch, F. A. Rey, D. Veesler,
1193   Tectonic conformational changes of a coronavirus spike glycoprotein promote membrane
1194   fusion. *Proc. Natl. Acad. Sci. U. S. A.* **114**, 11157–11162 (2017).

28. Y. Cai, J. Zhang, T. Xiao, H. Peng, S. M. Sterling, R. M. Walsh, S. Rawson, S. Rits-Volloch, B. Chen, Distinct conformational states of SARS-CoV-2 spike protein. *Science*. **369**, 1586–1592 (2020).

29. X. Fan, D. Cao, L. Kong, X. Zhang, Cryo-EM analysis of the post-fusion structure of the SARS-CoV spike glycoprotein. *Nat. Commun.* **11**, 3618 (2020).

30. F. A. Lempp, L. Soriaga, M. Montiel-Ruiz, F. Benigni, J. Noack, Y.-J. Park, S. Bianchi, A. C. Walls, J. E. Bowen, J. Zhou, H. Kaiser, M. Agostini, M. Meury, E. Dellota Jr, S. Jaconi, E. Cameroni, H. W. Virgin, A. Lanzavecchia, D. Veesler, L. Purcell, A. Telenti, D. Corti, Membrane lectins enhance SARS-CoV-2 infection and influence the neutralizing activity of different classes of antibodies. *bioRxiv* (2021), , doi:10.1101/2021.04.03.438258.

31. L. Piccoli, Y. J. Park, M. A. Tortorici, N. Czudnochowski, A. C. Walls, M. Beltramello, C. Silacci-Fregni, D. Pinto, L. E. Rosen, J. E. Bowen, O. J. Acton, S. Jaconi, B. Guarino, A. Minola, F. Zatta, N. Sprugasci, J. Bassi, A. Peter, A. De Marco, J. C. Nix, F. Mele, S. Jovic, B. F. Rodriguez, S. V. Gupta, F. Jin, G. Piumatti, G. Lo Presti, A. F. Pellanda, M. Biggiogero, M. Tarkowski, M. S. Pizzuto, E. Cameroni, C. Havenar-Daughton, M. Smithey, D. Hong, V. Lepori, E. Albanese, A. Ceschi, E. Bernasconi, L. Elzi, P. Ferrari, C. Garzoni, A. Riva, G. Snell, F. Sallusto, K. Fink, H. W. Virgin, A. Lanzavecchia, D. Corti, D. Veesler, Mapping Neutralizing and Immunodominant Sites on the SARS-CoV-2 Spike Receptor-Binding Domain by Structure-Guided High-Resolution Serology. *Cell*. **183**, 1024-1042.e21 (2020).

32. A. Schäfer, F. Muecksch, J. C. C. Lorenzi, S. R. Leist, M. Cipolla, S. Bournazos, F. Schmidt, R. M. Maison, A. Gazumyan, D. R. Martinez, R. S. Baric, D. F. Robbiani, T. Hatziioannou, J. V. Ravetch, P. D. Bieniasz, R. A. Bowen, M. C. Nussenzweig, T. P. Sheahan, Antibody potency, effector function, and combinations in protection and therapy for SARS-CoV-2 infection in vivo. *J. Exp. Med.* **218** (2021), doi:10.1084/jem.20201993.

33. S. Bournazos, T. T. Wang, J. V. Ravetch, The Role and Function of Fcγ Receptors on Myeloid Cells. *Microbiol Spectr*. **4** (2016), doi:10.1128/microbiolspec.MCHD-0045-2016.

34. S. Bournazos, D. Corti, H. W. Virgin, J. V. Ravetch, Fc-optimized antibodies elicit CD8 immunity to viral respiratory infection. *Nature*. **588**, 485–490 (2020).

35. E. S. Winkler, P. Gilchuk, J. Yu, A. L. Bailey, R. E. Chen, S. J. Zost, H. Jang, Y. Huang, J. D. Allen, J. B. Case, R. E. Sutton, R. H. Carnahan, T. L. Darling, A. C. M. Boon, M. Mack, R. D. Head, T. M. Ross, J. E. Crowe, M. Diamond, *bioRxiv*, in press.

36. R. Boudewijns, H. J. Thibaut, S. J. F. Kaptein, R. Li, V. Vergote, L. Seldeslachts, J. Van Weyenbergh, C. De Keyzer, L. Bervoets, S. Sharma, L. Liesenborghs, J. Ma, S. Jansen, D. Van Looveren, T. Vercruysse, X. Wang, D. Jochmans, E. Martens, K. Roose, D. De Vlieger, B. Schepens, T. Van Buyten, S. Jacobs, Y. Liu, J. Martí-Carreras, B. Vanmechelen, T. Wawina-Bokalanga, L. Delang, J. Rocha-Pereira, L. Coelmont, W. Chiu, P. Leyssen, E. Heylen, D. Schols, L. Wang, L. Close, J. Matthijnssens, M. Van Ranst, V. Compernolle, G. Schramm, K. Van Laere, X. Saelens, N. Callewaert, G. Opdenakker, P. Maes, B. Weynand, C. Cawthorne, G. Vande Velde, Z. Wang, J. Neyts, K. Dallmeier, STAT2 signaling restricts viral dissemination but drives severe pneumonia in SARS-CoV-2 infected hamsters. *Nat. Commun.* **11**, 5838 (2020).

1237   37.   J. Tan, B. K. Sack, D. Oyen, I. Zenklusen, L. Piccoli, S. Barbieri, M. Foglierini, C. S. Fregni,
1238   J. Marcandalli, S. Jongo, S. Abdulla, L. Perez, G. Corradin, L. Varani, F. Sallusto, B. K. L.
1239   Sim, S. L. Hoffman, S. H. I. Kappe, C. Daubenberger, I. A. Wilson, A. Lanzavecchia, A
1240   public antibody lineage that potently inhibits malaria infection through dual binding to the
1241   circumsporozoite protein. *Nat. Med.* **24**, 401–407 (2018).

1242   38.   D. Pinna, D. Corti, D. Jarrossay, F. Sallusto, A. Lanzavecchia, Clonal dissection of the
1243   human memory B-cell repertoire following infection and vaccination. *Eur. J. Immunol.* **39**,
1244   1260–1270 (2009).

1245   39.   C. Daniel, R. Anderson, M. J. Buchmeier, J. O. Fleming, W. J. Spaan, H. Wege, P. J.
1246   Talbot, Identification of an immunodominant linear neutralization domain on the S2 portion
1247   of the murine coronavirus spike glycoprotein and evidence that it forms part of complex
1248   tridimensional structure. *J. Virol.* **67**, 1185–1194 (1993).

1249   40.   H. Zhang, G. Wang, J. Li, Y. Nie, X. Shi, G. Lian, W. Wang, X. Yin, Y. Zhao, X. Qu, M.
1250   Ding, H. Deng, Identification of an antigenic determinant on the S2 domain of the severe
1251   acute respiratory syndrome coronavirus spike glycoprotein capable of inducing neutralizing
1252   antibodies. *J. Virol.* **78**, 6938–6945 (2004).

1253   41.   C. M. Poh, G. Carissimo, B. Wang, S. N. Amrun, C. Y. Lee, R. S. Chee, S. W. Fong, N. K.
1254   Yeo, W. H. Lee, A. Torres-Ruesta, Y. S. Leo, M. I. Chen, S. Y. Tan, L. Y. A. Chai, S.
1255   Kalimuddin, S. S. G. Kheng, S. Y. Thien, B. E. Young, D. C. Lye, B. J. Hanson, C. I. Wang,
1256   L. Renia, L. F. P. Ng, Two linear epitopes on the SARS-CoV-2 spike protein that elicit
1257   neutralising antibodies in COVID-19 patients. *Nat. Commun.* **11**, 2806 (2020).

1258   42.   H. A. Elshabrawy, M. M. Coughlin, S. C. Baker, B. S. Prabhakar, Human monoclonal
1259   antibodies against highly conserved HR1 and HR2 domains of the SARS-CoV spike
1260   protein are more broadly neutralizing. *PLoS One*. **7**, e50366 (2012).

1261   43.   Z. Zheng, V. M. Monteil, S. Maurer-Stroh, C. W. Yew, C. Leong, N. K. Mohd-Ismail, S.
1262   Cheyyatraivendran Arularasu, V. T. K. Chow, R. T. P. Lin, A. Mirazimi, W. Hong, Y. J. Tan,
1263   Monoclonal antibodies for the S2 subunit of spike of SARS-CoV-1 cross-react with the
1264   newly-emerged SARS-CoV-2. *Euro Surveill.* **25** (2020), doi:10.2807/1560-
1265   7917.ES.2020.25.28.2000291.

1266   44.   A. C. Walls, M. A. Tortorici, B. J. Bosch, B. Frenz, P. J. M. Rottier, F. DiMaio, F. A. Rey, D.
1267   Veesler, Cryo-electron microscopy structure of a coronavirus spike glycoprotein trimer.
1268   *Nature*. **531**, 114–117 (2016).

1269   45.   P. Zhou, M. Yuan, G. Song, N. Beutler, N. Shaabani, D. Huang, W.-T. He, X. Zhu, S.
1270   Callaghan, P. Yong, F. Anzanello, L. Peng, J. Ricketts, M. Parren, E. Garcia, S. A.
1271   Rawlings, D. M. Smith, D. Nemazee, J. R. Teijaro, T. F. Rogers, I. A. Wilson, D. R. Burton,
1272   R. Andrabi, A protective broadly cross-reactive human antibody defines a conserved site of
1273   vulnerability on beta-coronavirus spikes. *bioRxivorg* (2021),
1274   doi:10.1101/2021.03.30.437769.

1275   46.   D. Corti, J. Voss, S. J. Gamblin, G. Codoni, A. Macagno, D. Jarrossay, S. G. Vachieri, D.
1276   Pinna, A. Minola, F. Vanzetta, C. Silacci, B. M. Fernandez-Rodriguez, G. Agatic, S.
1277   Bianchi, I. Giacchetto-Sasselli, L. Calder, F. Sallusto, P. Collins, L. F. Haire, N. Temperton,
1278   J. P. Langedijk, J. J. Skehel, A. Lanzavecchia, A neutralizing antibody selected from

1279   plasma cells that binds to group 1 and group 2 influenza A hemagglutinins. *Science*. **333**,
1280   850–856 (2011).

1281   47.   D. J. DiLillo, G. S. Tan, P. Palese, J. V. Ravetch, Broadly neutralizing hemagglutinin stalk-
1282   specific antibodies require FcγR interactions for protection against influenza virus in vivo.
1283   *Nat. Med.* **20**, 143–151 (2014).

1284   48.   D. Corti, A. L. Suguitan Jr, D. Pinna, C. Silacci, B. M. Fernandez-Rodriguez, F. Vanzetta,
1285   C. Santos, C. J. Luke, F. J. Torres-Velez, N. J. Temperton, R. A. Weiss, F. Sallusto, K.
1286   Subbarao, A. Lanzavecchia, Heterosubtypic neutralizing antibodies are produced by
1287   individuals immunized with a seasonal influenza vaccine. *J. Clin. Invest.* **120**, 1663–1673
1288   (2010).

1289   49.   F. Sesterhenn, C. Yang, J. Bonet, J. T. Cramer, X. Wen, Y. Wang, C. I. Chiang, L. A.
1290   Abriata, I. Kucharska, G. Castoro, S. S. Vollers, M. Galloux, E. Dheilly, S. Rosset, P.
1291   Corthésy, S. Georgeon, M. Villard, C. A. Richard, D. Descamps, T. Delgado, E. Oricchio,
1292   M. A. Rameix-Welti, V. Más, S. Ervin, J. F. Eléouët, S. Riffault, J. T. Bates, J. P. Julien, Y.
1293   Li, T. Jardetzky, T. Krey, B. E. Correia, De novo protein design enables the precise
1294   induction of RSV-neutralizing antibodies. *Science*. **368** (2020),
1295   doi:10.1126/science.aay5051.

1296   50.   M. L. Azoitei, B. E. Correia, Y. E. Ban, C. Carrico, O. Kalyuzhniy, L. Chen, A. Schroeter, P.
1297   S. Huang, J. S. McLellan, P. D. Kwong, D. Baker, R. K. Strong, W. R. Schief, Computation-
1298   guided backbone grafting of a discontinuous motif onto a protein scaffold. *Science*. **334**,
1299   373–376 (2011).

1300   51.   B. E. Correia, J. T. Bates, R. J. Loomis, G. Baneyx, C. Carrico, J. G. Jardine, P. Rupert, C.
1301   Correnti, O. Kalyuzhniy, V. Vittal, M. J. Connell, E. Stevens, A. Schroeter, M. Chen, S.
1302   Macpherson, A. M. Serra, Y. Adachi, M. A. Holmes, Y. Li, R. E. Klevit, B. S. Graham, R. T.
1303   Wyatt, D. Baker, R. K. Strong, J. E. Crowe, P. R. Johnson, W. R. Schief, Proof of principle
1304   for epitope-focused vaccine design. *Nature*. **507**, 201–206 (2014).

1305   52.   A. C. Walls, B. Fiala, A. Schäfer, S. Wrenn, M. N. Pham, M. Murphy, L. V. Tse, L. Shehata,
1306   M. A. O'Connor, C. Chen, M. J. Navarro, M. C. Miranda, D. Pettie, R. Ravichandran, J. C.
1307   Kraft, C. Ogohara, A. Palser, S. Chalk, E. C. Lee, K. Guerriero, E. Kepl, C. M. Chow, C.
1308   Sydeman, E. A. Hodge, B. Brown, J. T. Fuller, K. H. Dinnon, L. E. Gralinski, S. R. Leist, K.
1309   L. Gully, T. B. Lewis, M. Guttman, H. Y. Chu, K. K. Lee, D. H. Fuller, R. S. Baric, P. Kellam,
1310   L. Carter, M. Pepper, T. P. Sheahan, D. Veesler, N. P. King, Elicitation of Potent
1311   Neutralizing Antibody Responses by Designed Protein Nanoparticle Vaccines for SARS-
1312   CoV-2. *Cell*. **183**, 1367-1382.e17 (2020).

1313   53.   A. C. Walls, M. C. Miranda, M. N. Pham, A. Schäfer, A. Greaney, P. S. Arunachalam, M.-J.
1314   Navarro, M. A. Tortorici, K. Rogers, M. A. O'Connor, L. Shireff, D. E. Ferrell, N. Brunette, E.
1315   Kepl, J. Bowen, S. K. Zepeda, T. Starr, C.-L. Hsieh, B. Fiala, S. Wrenn, D. Pettie, C.
1316   Sydeman, M. Johnson, A. Blackstone, R. Ravichandran, C. Ogohara, L. Carter, S. W.
1317   Tilles, R. Rappuoli, D. T. O'Hagan, R. Van Der Most, W. C. Van Voorhis, J. S. McLellan, H.
1318   Kleanthous, T. P. Sheahan, D. H. Fuller, F. Villinger, J. Bloom, B. Pulendran, R. Baric, N.
1319   King, D. Veesler, Elicitation of broadly protective sarbecovirus immunity by receptor-
1320   binding domain nanoparticle vaccines. *bioRxivorg* (2021), doi:10.1101/2021.03.15.435528.

54. S. Boyoglu-Barnum, D. Ellis, R. A. Gillespie, G. B. Hutchinson, Y.-J. Park, S. M. Moin, O. J. Acton, R. Ravichandran, M. Murphy, D. Pettie, N. Matheson, L. Carter, A. Creanga, M. J. Watson, S. Kephart, S. Ataca, J. R. Vaile, G. Ueda, M. C. Crank, L. Stewart, K. K. Lee, M. Guttman, D. Baker, J. R. Mascola, D. Veesler, B. S. Graham, N. P. King, M. Kanekiyo, Quadrivalent influenza nanoparticle vaccines induce broad protection. *Nature* (2021), doi:10.1038/s41586-021-03365-x.

55. M. Kanekiyo, C. J. Wei, H. M. Yassine, P. M. McTamney, J. C. Boyington, J. R. Whittle, S. S. Rao, W. P. Kong, L. Wang, G. J. Nabel, Self-assembling influenza nanoparticle vaccines elicit broadly neutralizing H1N1 antibodies. *Nature*. **499**, 102–106 (2013).

56. M. Kanekiyo, M. G. Joyce, R. A. Gillespie, J. R. Gallagher, S. F. Andrews, H. M. Yassine, A. K. Wheatley, B. E. Fisher, D. R. Ambrozak, A. Creanga, K. Leung, E. S. Yang, S. Boyoglu-Barnum, I. S. Georgiev, Y. Tsybovsky, M. S. Prabhakaran, H. Andersen, W. P. Kong, U. Baxa, K. L. Zephir, J. E. Ledgerwood, R. A. Koup, P. D. Kwong, A. K. Harris, A. B. McDermott, J. R. Mascola, B. S. Graham, Mosaic nanoparticle display of diverse influenza virus hemagglutinins elicits broad B cell responses. *Nat. Immunol.* **20**, 362–372 (2019).

57. J. Marcandalli, B. Fiala, S. Ols, M. Perotti, W. de van der Schueren, J. Snijder, E. Hodge, M. Benhaim, R. Ravichandran, L. Carter, W. Sheffler, L. Brunner, M. Lawrenz, P. Dubois, A. Lanzavecchia, F. Sallusto, K. K. Lee, D. Veesler, C. E. Correnti, L. J. Stewart, D. Baker, K. Lore, L. Perez, N. P. King, Induction of Potent Neutralizing Antibody Responses by a Designed Protein Nanoparticle Vaccine for Respiratory Syncytial Virus. *Cell*. **176**, 1420-1431 e17 (2019).

58. M. A. Tortorici, N. Czudnochowski, T. N. Starr, R. Marzi, A. C. Walls, F. Zatta, J. E. Bowen, S. Jaconi, J. di Iulio, Z. Wang, A. De Marco, S. K. Zepeda, D. Pinto, Z. Liu, M. Beltramello, I. Bartha, M. P. Housley, F. A. Lempp, L. E. Rosen, E. Dellota, H. Kaiser, M. Montiel-Ruiz, J. Zhou, A. Addetia, B. Guarino, K. Culap, N. Sprugasci, C. Saliba, E. Vetti, I. Giacchetto-Sasselli, C. S. Fregni, R. Abdelnabi, S.-Y. C. Foo, C. Havenar-Daughton, M. A. Schmid, F. Benigni, E. Cameroni, J. Neyts, A. Telenti, G. Snell, H. W. Virgin, S. P. J. Whelan, J. D. Bloom, D. Corti, D. Veesler, M. S. Pizzuto, Structural basis for broad sarbecovirus neutralization by a human monoclonal antibody. *bioRxivorg* (2021), doi:10.1101/2021.04.07.438818.

59. M. A. Tortorici, A. C. Walls, Y. Lang, C. Wang, Z. Li, D. Koerhuis, G. J. Boons, B. J. Bosch, F. A. Rey, R. J. de Groot, D. Veesler, Structural basis for human coronavirus attachment to sialic acid receptors. *Nat. Struct. Mol. Biol.* **26**, 481–489 (2019).

60. Y. J. Park, A. C. Walls, Z. Wang, M. M. Sauer, W. Li, M. A. Tortorici, B. J. Bosch, F. DiMaio, D. Veesler, Structures of MERS-CoV spike glycoprotein in complex with sialoside attachment receptors. *Nat. Struct. Mol. Biol.* **26**, 1151–1157 (2019).

61. T. N. Starr, N. Czudnochowski, F. Zatta, Y.-J. Park, Z. Liu, A. Addetia, D. Pinto, M. Beltramello, P. Hernandez, A. J. Greaney, R. Marzi, W. G. Glass, I. Zhang, A. S. Dingens, J. E. Bowen, J. A. Wojcechowskyj, A. De Marco, L. E. Rosen, J. Zhou, M. Montiel-Ruiz, H. Kaiser, H. Tucker, M. P. Housley, J. di Iulio, G. Lombardo, M. Agostini, N. Sprugasci, K. Culap, S. Jaconi, M. Meury, E. Dellota, E. Cameroni, T. I. Croll, J. C. Nix, C. Havenar-Daughton, A. Telenti, F. A. Lempp, M. S. Pizzuto, J. D. Chodera, C. M. Hebner, S. P. J. Whelan, H. W. Virgin, D. Veesler, D. Corti, J. D. Bloom, G. Snell, Antibodies to the SARS-

1365   CoV-2 receptor-binding domain that maximize breadth and resistance to viral escape.
1366   *bioRxivorg* (2021), doi:10.1101/2021.04.06.438709.

1367   62.   A. M. Bolger, M. Lohse, B. Usadel, Trimmomatic: a flexible trimmer for Illumina sequence
1368   data. *Bioinformatics*. **30**, 2114–2120 (2014).

1369   63.   H. Li, Aligning sequence reads, clone sequences and assembly contigs with BWA-MEM.
1370   *arXiv [q-bio.GN]* (2013), (available at http://arxiv.org/abs/1303.3997).

1371   64.   A. Wilm, P. P. K. Aw, D. Bertrand, G. H. T. Yeo, S. H. Ong, C. H. Wong, C. C. Khor, R.
1372   Petric, M. L. Hibberd, N. Nagarajan, LoFreq: a sequence-quality aware, ultra-sensitive
1373   variant caller for uncovering cell-population heterogeneity from high-throughput sequencing
1374   datasets. *Nucleic Acids Res.* **40**, 11189–11201 (2012).

1375   65.   P. Cingolani, A. Platts, L. L. Wang, M. Coon, T. Nguyen, L. Wang, S. J. Land, X. Lu, D. M.
1376   Ruden, A program for annotating and predicting the effects of single nucleotide
1377   polymorphisms, SnpEff: SNPs in the genome of Drosophila melanogaster strain w1118;
1378   iso-2; iso-3. *Fly (Austin)*. **6**, 80–92 (2012).

1379   66.   B. S. Pedersen, A. R. Quinlan, Mosdepth: quick coverage calculation for genomes and
1380   exomes. *Bioinformatics*. **34**, 867–868 (2018).

1381   67.   P. Danecek, J. K. Bonfield, J. Liddle, J. Marshall, V. Ohan, M. O. Pollard, A. Whitwham, T.
1382   Keane, S. A. McCarthy, R. M. Davies, H. Li, Twelve years of SAMtools and BCFtools.
1383   *Gigascience*. **10** (2021), doi:10.1093/gigascience/giab008.

1384   68.   P. Ewels, M. Magnusson, S. Lundin, M. Käller, MultiQC: summarize analysis results for
1385   multiple tools and samples in a single report. *Bioinformatics*. **32**, 3047–3048 (2016).

1386   69.   P. Di Tommaso, M. Chatzou, E. W. Floden, P. P. Barja, E. Palumbo, C. Notredame,
1387   Nextflow enables reproducible computational workflows. *Nat. Biotechnol.* **35**, 316–319
1388   (2017).

1389   70.   B. Grüning, R. Dale, A. Sjödin, B. A. Chapman, J. Rowe, C. H. Tomkins-Tinch, R. Valieris,
1390   J. Köster, Bioconda Team, Bioconda: sustainable and comprehensive software distribution
1391   for the life sciences. *Nat. Methods*. **15**, 475–476 (2018).

1392   71.   P. Emsley, B. Lohkamp, W. G. Scott, K. Cowtan, Features and development of Coot. *Acta
1393   Crystallogr. D Biol. Crystallogr.* **66**, 486–501 (2010).

1394   72.   T. I. Croll, ISOLDE: a physically realistic environment for model building into low-resolution
1395   electron-density maps. *Acta Crystallogr D Struct Biol*. **74**, 519–530 (2018).

1396   73.   G. N. Murshudov, P. Skubák, A. A. Lebedev, N. S. Pannu, R. A. Steiner, R. A. Nicholls, M.
1397   D. Winn, F. Long, A. A. Vagin, REFMAC5 for the refinement of macromolecular crystal
1398   structures. *Acta Crystallogr. D Biol. Crystallogr.* **67**, 355–367 (2011).

1399   74.   C. Suloway, J. Pulokas, D. Fellmann, A. Cheng, F. Guerra, J. Quispe, S. Stagg, C. S.
1400   Potter, B. Carragher, Automated molecular microscopy: the new Leginon system. *J. Struct.
1401   Biol.* **151**, 41–60 (2005).

1402 75. D. Tegunov, P. Cramer, Real-time cryo-electron microscopy data preprocessing with Warp.
1403   *Nat. Methods*. **16**, 1146–1152 (2019).

1404 76. A. Punjani, J. L. Rubinstein, D. J. Fleet, M. A. Brubaker, cryoSPARC: algorithms for rapid
1405   unsupervised cryo-EM structure determination. *Nat. Methods*. **14**, 290–296 (2017).

1406 77. J. Zivanov, T. Nakane, S. H. W. Scheres, A Bayesian approach to beam-induced motion
1407   correction in cryo-EM single-particle analysis. *IUCrJ*. **6**, 5–17 (2019).

1408 78. S. Chen, G. McMullan, A. R. Faruqi, G. N. Murshudov, J. M. Short, S. H. Scheres, R.
1409   Henderson, High-resolution noise substitution to measure overfitting and validate resolution
1410   in 3D structure determination by single particle electron cryomicroscopy. *Ultramicroscopy*.
1411   **135**, 24–35 (2013).

1412 79. E. F. Pettersen, T. D. Goddard, C. C. Huang, G. S. Couch, D. M. Greenblatt, E. C. Meng,
1413   T. E. Ferrin, UCSF Chimera--a visualization system for exploratory research and analysis.
1414   *J. Comput. Chem.* **25**, 1605–1612 (2004).

1415 80. L. J. Reed, H. Muench, A SIMPLE METHOD OF ESTIMATING FIFTY PER CENT
1416   ENDPOINTS12. *Am. J. Epidemiol.* **27**, 493–497 (1938).

1417 81. M. Foglierini, L. Pappas, A. Lanzavecchia, D. Corti, L. Perez, AncesTree: An interactive
1418   immunoglobulin lineage tree visualizer. *PLoS Comput. Biol.* **16**, e1007731 (2020).